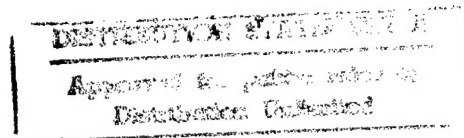FINAL REPORT

LOAD TRANSFER CHARACTERISTICS AND RESIDUAL STRESSES IN COMPOSITE MATERIAL SYSTEMS

by

E. S. Folias

Submitted to

AIR FORCE OFFICE OF SCIENTIFIC RESEARCH

Department of Mathematics
University of Utah
Salt Lake City, Utah 84112

February 1997

19970616 094

FINAL REPORT

LOAD TRANSFER CHARACTERISTICS AND RESIDUAL STRESSES IN COMPOSITE MATERIAL SYSTEMS

by

E. S. Folias

Department of Mathematics
University of Utah
Salt Lake City, Utah 84112

February 1997

PREFACE

Titanium matrix composites reinforced with SIC fibers have been the subject of extensive research over the past decade because of interest in advanced aerospace applications that require light weight, high stiffness, and high temperature capabilities. Programs such as the National Aerospace Plane (NASP) and the Air Force Integrated High Performance Turbine Engine Technology (IHPTET), in particular, have been evaluating the properties, mechanical behavior, and failure mechanisms of this class of materials under typical anticipated use conditions. While failure modes depend on the specific mechanical and thermal loading conditions, fiber failure has been identified as either a direct mode of failure or as a dominant mode of failure after some other mode such as matrix cracking has produced an increase in fiber stresses.

Direct failure of fibers which act as a bundle embedded in a ductile matrix material is considered to be the primary cause of composite material failure under creep, low cycle fatigue, and in-phase thermo-mechanical fatigue (IP TMF). The process of breakage of the fiber bundle, however, is not very well understood. Results of IP TMF tests on composites with SiC fibers having different matrix materials, and tested at different maximum temperatures, show apparently different modes of progressive failure after a fiber has broken. Timetal matrix composites at 650 C maximum temperature show debonding of the fiber/matrix interface in the region adjacent to the fiber crack. Ti-6-1-4V composites at 427 C, on the other hand, show an apparent propensity for matrix cracking adjacent to the fiber break. To evaluate the potential for forming an interface crack, and to shed light on the mechanics of crack formation and interfacial toughness, the present study was undertaken. The analysis refrains from making many of the simplifying assumptions about stress distributions which are commonly utilized in analyses of this type. Instead, a rigorous and systematic elastic analysis is conducted using only the boundary conditions as an"assumption" in addressing the problem. Moreover, the general problem is broken down into key problems which are examined individually and will finally be combined to provide answers to the general problem.

It was found convenient to divide the work into two different parts.

In part I, we examine the load transfer characteristics of a material system after a fiber breaks.

In part II, we examine the residual stresses due to curing and thermal stresses due to differences between the thermal expansion coefficients of the matrix and fiber.

In part III, we are developing a *sinc-function based numerical method* that is geared specifically for solving 3D problems that posses stress singularities, in certain regions of the body.

PART I

LOAD TRANSFER CHARACTERISTICS IN METAL / MATRIX COMPOSITES DUE TO A FIBER BREAKAGE

by

E. S. Folias

University of Utah, Department of Mathematics, Salt lake City, Utah, 84112.

January 1997

ABSTRACT

In this study, the load transfer characteristics of a broken fiber are investigated. The problem consists of a cylindrical fiber that is embedded into a matrix material. The fiber axis is assumed to coincide with the z-axis and a crack is assumed to be present on the plane $z = 0$ and for $r < a$. Far away from the crack, the fiber is subjected to uniform external load of σ_o.

Moreover, adjacent to the crack and along the interface (see fig. 3), the matrix and fiber surfaces are assumed to slide along the interface length $-c < z < c$, in the presence of a variable friction $\tau_{rz}^{(f)} = \mu \sigma_{rr}^{(m)}$. On the other hand, perfect bonding is assumed to prevail all along the remaining interface, i.e. for $|z| > c$.

For the solution of the problem, we utilize a Fourier Integral Transform whereby we reduce the problem to that of the solution of a singular integral equation along the interface path $-c < z < c$. The solution of this integral equation then allows the determination of the displacement and stress fields. Two areas of special interest immediately come to mind, (i) the neighborhood adjacent to the point $|z| = c$ and $r = a$, and (ii) the neighborhood adjacent to the point $z = 0$ and $r = a$.

The analysis reveals that the load transfer characteristics depend heavily on the material properties of the system.

1. Introduction

It is well recognized that realistic modeling of deformation and damage accumulation in the fatigue of metal-matrix composites depends heavily on the mechanisms which govern the damage. Experimental evidence of the accumulation of strain in a SiC-fiber/titanium-matrix composite, in conjunction with fractographic examination of the samples, point to fiber breakage as the dominant mode of failure during thermomechanical fatigue tests. During this physical process individual fibers break periodically, at random locations, and throughout the composite. Considerable work on the modeling of broken fibers in composites has already been conducted over a number of years. In the literature one may find the work of Rosen (1964) using a shear- lag model. The stress concentration present in the immediate vicinity of a broken fiber was first analyzed by Hedgepeth (1961) and has subsequently been addressed by many others who have utilized other simpler models. Recently, Penado and Folias (1989) investigated the stress concentrations in a fiber based on three dimensional considerations. Moreover, the 3D edge effects, when a fiber meets a free surface, have been investigated by Folias (1989). A closer inspection, however, of the local neighborhood of a fractured fiber (see Fig. 1) reveals that the problem is much more difficult that it was originally thought of. This is because one must also account for the vertical interface cracks that develop along the sides of the fiber. One may also recall the fact that composites, in general, are attractive in using them for practical applications because the fibers are designed to carry most of the applied load. Consequently, when a fiber breaks, at least locally, the load must then be transferred somehow to the other portion of the broken fiber via the matrix. This suggests, therefore, that the adjacent matrix must now carry a much higher stress load. In reality, however, one may conjecture that (i) there is some redistribution of the load to the adjacent unbroken fibers, and that (ii) there is perhaps an increase in the load which the adjacent matrix must now carry. Recently, Nicholas and Ahmad (1994), through the analysis of a relatively simple model, were able to provide some qualitative answers regarding this complex phenomenon. On the other hand, a more sophisticated stress analysis of the local problem, coupled with the results of a sporadic sequence of fiber breaks along the composite material system, can provide important information and guidance to material designers for the development of future material systems.

2. Formulation of the Problem

Consider the equilibrium of a material system that occupies the space $|x| < \infty$, $|y| < \infty$, $|z| < \infty$ and contains a cylindrical fiber that is embedded into a matrix space (see Fig. 1). The fiber axis coincides with the z-axes and the fiber radius is $r = a$. Both fiber and matrix materials are assumed to be homogeneous, isotropic and linearly elastic. At the interface ($r = a$) perfect bonding is assumed to prevail.

In this model, we envision the failure to take place in three different stages. During the first stage, a plane crack is formed in the middle of the fiber region, i.e. at $r < a$ and on the plane $z = 0$, and advances until it reaches the fiber/matrix interface boundary. This problem has been studied by others and recently more rigorously by Pagano et al (1995). Subsequently, during the second stage, a certain length along the fiber/matrix interface, above and bellow the plane $z = 0$, has debonded and the matrix is now allowed to slip in the presence of a non-constant frictional

force. Finally, during the third stage, the fiber crack pups open and a finite jump in the fiber displacement is formed. The present analysis deals with the events of the second stage. We believe that the analysis of this stage will provide important information related to the failure process and may reveal 'the sufficient conditions' required for the subsequent advancement of the failure to that of stage three. Putting it another way, it is hoped that it will reveal the ' sufficient conditions ' required to suppress any further development of the failure.

At a certain instant in time, the fiber breaks in two peaces as shown in Figs 2 and 3. The separation distance Δ_o , denotes the maximum displacement between the fiber faces after the system has been loaded. It is also assumed that, subsequent to the fiber breakage, splitting between fiber and matrix along the interface and up to a distance $-c < z < c$ is simultaneously being formed in the presence of a non-uniform frictional force. As to loading, far away from the location of the break, the fiber carries a uniform stress σ_0 parallel to the direction of the fiber axis. Similarly, the matrix carries a uniform stress σ_1 also in the direction of the fiber axis.

In the absence of body forces, the differential equation governing the stress potential functions $\Phi^{(f)}$ and $\Phi^{(m)}$ is given by

$$\nabla^4\Phi = 0 \qquad\qquad (1)$$

where ∇^4 is the biharmonic operator. The displacement and stress fields are then given in terms of the potential functions as :

(i) displacement field :

$$2Gu_r = -\frac{\partial^2\Phi}{\partial r\partial z} \qquad\qquad (2)$$

$$2Gw = 2(1-v)\nabla^2\Phi - \frac{\partial^2\Phi}{\partial z^2} \qquad\qquad (3)$$

(ii) stress field :

$$\sigma_{rr} = v\nabla^2\frac{\partial\Phi}{\partial z} - \frac{\partial^3\Phi}{\partial r^2\partial z} \qquad\qquad (4)$$

$$\sigma_{zz} = (2-v)\nabla^2\frac{\partial\Phi}{\partial z} - \frac{\partial^3\Phi}{\partial z^3} \qquad\qquad (5)$$

$$\tau_{rz} = (1-v)\nabla^2\frac{\partial\Phi}{\partial r} - \frac{\partial^3\Phi}{\partial r\partial z^2} \qquad\qquad (6)$$

where v is Poisson's ratio and G the shear modulus.

As to boundary conditions, we require that :

2

(i) matrix region :

at $z = 0$: $\quad w^{(m)} = 0$ $\qquad\qquad\qquad\qquad\qquad$ (7)

at $z = 0$: $\quad \tau_{rz}^{(m)} = 0$ $\qquad\qquad\qquad\qquad\qquad$ (8)

(ii) fiber region :

at $z = 0$: $\quad \tau_{rz}^{(f)} = 0$ $\qquad\qquad\qquad\qquad\qquad$ (9)

at $z = 0$: $\quad \int_0^a 2\pi r \sigma_{zz}^{(f)} dr = 0$ $\qquad\qquad\qquad$ (10)

at $z = 0$: $\quad w^{(f)}(r, 0) = \Delta_o \sqrt{a^2 - r^2}$ $\qquad\quad$ (11)

It may be noted here that the latter represents a crack that has the shape of a very sharp ellipse. In this study, the primary emphasis was to examine the effect that a non-uniform frictional force has on the mechanism of failure and to gain some further insight on the evolution of the events of this complex crack formation. In a follow up paper, which the authors are presently working on, the boundary conditions have been relaxed by allowing now the fiber displacement w to possess a finite jump.

(iii) interface region :

at $r = a$: $\quad u_r^{(f)} = u_r^{(m)}$ $\qquad\quad$; $0 < z < \infty$ $\qquad$ (12)

at $r = a$: $\quad \sigma_{rr}^{(f)} = \sigma_{rr}^{(m)}$ $\qquad\quad$; $0 < z < \infty$ $\qquad$ (13)

at $r = a$: $\quad w^{(f)} = w^{(m)}$ $\qquad\quad$; $0 < z < \infty$ $\qquad$ (14)

at $r = a$: $\quad \tau_{rz}^{(f)} = \tau_{rz}^{(m)}$ $\qquad\quad$; $c < z < \infty$ $\qquad$ (15)

at $r = a$: $\quad \tau_{rz}^{(f)} = \mu \sigma_{rr}^{(m)}$ $\qquad\quad$; $0 < z < c$ $\qquad$ (16)

Perhaps it may be appropriate here to note that one of the difficulties presented by boundary condition (16) is that the shear stress $\tau_{rz}^{(f)}$ is an odd function of z while the normal stress $\sigma_{rr}^{(m)}$ is an even function of z . At first glance this appears to be O.K., however the mathematical satisfaction of such type of a boundary condition requires some very special attention.

(iv) far away from the plane z = 0 :

$$\sigma_{zz}^{(f)} = \sigma_o \qquad\qquad\qquad\qquad\qquad (17)$$

3

$$\sigma_{zz}^{(m)} = \sigma_1 \qquad (18)$$

where σ_1 is related to σ_o via the relation :

$$\lim_{|z| \to \infty}(\varepsilon_{zz}^{(f)} - \varepsilon_{zz}^{(m)}) = 0 \qquad (19)$$

Moreover, in order to complete the formulation of the problem we must require that :

as r & z $\to \infty$: all complementary displacement and stresses must vanish

and the continuity condition :

at r = 0 : all the complementary displacements and stresses for the fiber must be bounded

3. Method of Solution

Without going into the mathematical details, we have constructed the following stress potential functions that exhibit the proper behavior at infinity.

$$\Phi^{(f)} = \int_0^\infty \{A^{(f)}I_o(sr) + B^{(f)}(sr)I_1(sr)\}\sin(sz)ds$$

$$\pm \sum_{n=0}^{\infty} \{C_n^{(f)} + D_n^{(f)}\alpha_n|z|\}\exp(-\alpha_n|z|)J_o(\alpha_n r) \qquad (20)$$

$$+ a^{(f)}z^3 + b^{(f)}zr^2$$

where the upper sign refers to $z > 0$ and the lower sign refers to $z < 0$,

$$den = 2G_f\nu_m - G_m\nu_f - G_f\nu_f(1 - 2\nu_m) - G_f + G_m - 2\nu_f\nu_m G_m \qquad (21)$$

$$a^{(f)} = -\frac{\sigma_o}{6(den)}\{4G_m\nu_m(1 - \nu_f) - 2G_f(\nu_m + \nu_f) + 4\nu_m\nu_f G_f$$

$$+ G_f - G_m\} \qquad (22)$$

$$b^{(f)} = \frac{\sigma_o}{2(den)}\{-\nu_f G_f(1 - 2\nu_m) + \nu_m G_m(1 - 2\nu_f)\} \qquad (23)$$

and

$$\Phi^{(m)} = \int_0^\infty \{A^{(m)}K_o(sr) + B^{(m)}(sr)K_1(sr)\}\sin(sz)ds$$

$$+ a^{(m)}z^3 + b^{(m)}zr^2 \qquad (24)$$

4

with

$$a^{(m)} = -\frac{\sigma_o}{6(den)}\{4\nu_m\nu_f(G_f - G_m) - 4\nu_f G_f + 2G_m(\nu_f - \nu_m)$$

$$+ G_f - G_m\}\frac{G_m}{G_f} \tag{25}$$

$$b^{(m)} = \frac{\sigma_o}{2(den)}\{\nu_m G_m - \nu_f G_f + 2\nu_m\nu_f(G_f - G_m)\}\frac{G_m}{G_f} \tag{26}$$

The constants $A^{(f)}, B^{(f)}, C^{(f)}, D^{(f)}, A^{(m)}, B^{(m)}$ are to be determined from the boundary conditions of the problem.

By construction, boundary conditions (7)-(8) are automatically satisfied. Next, to satisfy boundary condition (9), we let

$$C_n^{(f)} = 2\nu_f D_n^{(f)} \tag{27}$$

Similarly, to satisfy boundary condition (10) we choose α_n , n = 0,1,2,... , to be the roots of the equation

$$J_1(\alpha_n a) = 0 \tag{28}$$

in view of which eq. (10) now reduces to

$$\int_0^\infty s^2[2(1 - \nu_f)B^{(f)} + A^{(f)}]I_1(sa) + saB^{(f)}I_o(sa)\} ds = -\frac{\sigma_o}{2}a. \tag{29}$$

We will suppress, at this time, the satisfaction of the above condition but will return to it at a later time.

Next from eq (11), we have

$$w^{(f)}(r, 0) = -\frac{(1-\nu_f)}{G_f} \sum_{n=0}^\infty \alpha_n^2 D_n^{(f)} J_o(\alpha_n r) = \Delta_o\sqrt{a^2 - r^2} \tag{30}$$

in view of which the coefficient $D_n^{(f)}$ may now be determined as

$$-\frac{(1-\nu_f)}{G_f}\alpha_n^2 D_n^{(f)} = \frac{\sqrt{2\pi}\,\Delta_o a}{J_o^2(\alpha_n a)}\frac{J_{\frac{3}{2}}(\alpha_n a)}{(\alpha_n a)^{\frac{3}{2}}}; \qquad n = 1, 2, 3, ... \tag{31a}$$

and

$$-\frac{(1-\nu_f)}{G_f}\alpha_o^2 D_o^{(f)} = \frac{2}{3}\Delta_o a \tag{31b}$$

5

Thus, the crack opening in the fiber region becomes a very sharp ellipse. Perhaps it may be appropriate here to note that the constant Δ_o has now been related, through eqs (29) and (31), to the applied load σ_o. Moreover, the matrix load stress σ_1 is related to the fiber load stress σ_o through the eq. (19). More specifically,

$$\sigma_1 = \{ \frac{G_m}{G_f} \frac{[-2G_m \nu_f - G_f + G_m + 2\nu_m \nu_f G_f - 2G_m \nu_f \nu_m + G_f \nu_m + G_m \nu_m]}{[2G_f \nu_m - G_m \nu_f - G_f \nu_f + 2\nu_m \nu_f G_f - G_f + G_m - 2\nu_f \nu_m G_m]} \} \sigma_o \quad . \tag{32}$$

Next, the boundary conditions at the interface $r = a$

$$u_r^{(f)} - u_r^{(m)} = 0 \tag{33}$$
$$\sigma_{rr}^{(f)} - \sigma_{rr}^{(m)} = 0 \tag{34}$$

become respectively,

$$\int_0^\infty s^2 \{ (sa)K_o(sa)B^{(m)} + K_1(sa)A^{(m)} + G(sa)I_o(sa)B^{(f)}$$

$$+ GI_1(sa)A^{(f)} \} \cos(sz)ds = 0 \tag{35}$$

and

$$\int_0^\infty s^2 \{ [I_1(sa) - (sa)I_o(sa)]A^{(f)} + [-(1 - 2\nu_f)(sa)I_o(sa)$$

$$-(sa)^2 I_1(sa)]B^{(f)} + [K_1(sa) + (sa)K_o(sa)]A^{(f)}$$

$$+ [-(1 - 2\nu_m)(sa)K_o(sa) + (sa)^2 K_1(sa)]B^{(m)} \} \cos(sz)ds =$$

$$= -\sum_{n=0}^\infty a\alpha_n^3 \{ 1 - \alpha_n|z| \} D_n^{(f)} J_o(\alpha_n a)\exp(-\alpha_n|z|) \tag{36}$$

Similarly, the boundary condition[1]

$$w^{(f)} - w^{(m)} = 0 \tag{37}$$

becomes

$$\int_0^\infty s^2 \{ I_o(sa)A^{(f)} + [4(1 - \nu_f)I_o(sa) + (sa)I_1(sa)]B^{(f)}$$

$$- GK_o(sa)A^{(m)} + [4(1 - \nu_m)GK_o(sa) - G(sa)K_1(sa)]B^{(m)} \} \tag{38}$$

$$\times \sin(sz)ds = \sum_{n=0}^\infty \{ 2(1 - \nu_f) + \alpha_n|z| \} \alpha_n^2 D_n^{(f)} J_o(\alpha_n a)\exp(-\alpha_n|z|)$$

---

[1]   See remark on top of page 3.

6

where we have adapted the definition

$$G = \frac{G_f}{G_m} \ .$$
(39)

In order to facilitate our subsequent discussion, we define

$$e = (sa)\frac{I_0(sa)}{I_1(sa)}; \quad e_t = (sa)\frac{K_0(sa)}{K_1(sa)}$$
(40 a,b)

and

$$A^{(f)} = \frac{\hat{A}^{(f)}}{I_1(sa)}; \quad B^{(f)} = \frac{\hat{B}^{(f)}}{I_1(sa)}$$
(41 a,b)

$$A^{(m)} = \frac{\hat{A}^{(m)}}{K_0(sa)}; \quad B^{(m)} = \frac{\hat{B}^{(m)}}{K_1(sa)}$$
(42 a,b)

In view of eqs (40 a,b), (41 a,b), (42 a,b), equations (35) - (36) and (38), by Fourier inversion, become respectively :

$$\hat{A}^{(f)} + e\hat{B}^{(f)} + G\hat{A}^{(m)} + Ge_t\hat{B}^{(m)} = 0$$
(43)

$$(1 - e)\hat{A}^{(f)} + [-(1 - 2\nu_f)e - (sa)^2]\hat{B}^{(f)} + (1 + e_t)\hat{A}^{(m)}$$

$$+[-(1 - 2\nu_m)e_t + (sa)^2]\hat{B}^{(m)} = \frac{2}{\pi}\frac{a}{s}\int_0^\infty \xi\frac{\partial U}{\partial \xi}\sin(s\xi)d\xi$$
(44)

and

$$e\hat{A}^{(f)} + [4(1 - \nu_f)e + (sa)^2]\hat{B}^{(f)} - Ge_t\hat{A}^{(m)}$$

$$+[4G(1 - \nu_f)e_t - G(sa)^2]\hat{B}^{(m)} = \frac{2}{\pi}\frac{a}{s}\int_0^\infty \{2(1 - \nu_f)U$$

$$-\xi\frac{\partial U}{\partial \xi}\}\sin(s\xi)d\xi$$
(45)

where we have made use of the definition

$$U(\xi) = \sum_{n=0}^\infty \alpha_n^2 D_n^{(f)}\exp(-\alpha_n|\xi|)J_0(\alpha_n a) \ .$$
(46)

The system of eqs. (43)- (46) may now be solved in terms of one of the unknowns, say $\hat{B}^{(m)}$.
More specifically,

7

$$\hat{A}^{(m)} = \frac{P_2}{P_1}\hat{B}^{(m)} + \frac{2}{\pi}\frac{a}{s}\frac{1}{P_1}\int_0^\infty \xi\frac{\partial U}{\partial \xi}\sin(s\xi)d\xi + \frac{2}{\pi}\frac{a}{s}\frac{P_3}{P_1}\int_0^\infty U\sin(s\xi)d\xi \qquad (47)$$

$$\hat{B}^{(f)} = -\frac{(1-G)(1+e_t)}{2(1-v_f)e}\hat{A}^{(m)} - \frac{[(1-G)(sa)^2-(1-G)(1-2v_m)e_t+2G(1-v_m)e_t]}{2(1-v_f)}\hat{B}^{(m)}$$

$$+\frac{2}{\pi}\frac{a}{s}\frac{1}{e}\int_0^\infty U\sin(s\xi)d\xi \qquad (48)$$

$$\hat{A}^{(f)} = -e\hat{B}^{(f)} - G\hat{A}^{(m)} - Ge_t\hat{B}^{(m)} \qquad (49)$$

where for simplicity we have adopted the following definitions :

$$P_1 = 1 - G + e_t + Ge + \frac{[(1-2v_f)e+(1-e)e+(sa)^2]}{2(1-v_f)}(1-G)(\frac{1}{e} + \frac{e_t}{e}) \qquad (50)$$

$$P_2 = -(sa)^2 + (1-2v_m)e_t - G(1-e)e_t - \frac{[(1-2v_f)e+e(1-e)+(sa)^2]}{2(1-v_f)e}$$

$$\times\frac{[(1-G)(sa)^2-(1-G)(1-2v_m)e_t+2G(1-v_m)e_t]}{1} \qquad (51)$$

$$P_3 = \frac{[(1-2v_f)e+e(1-e)+(sa)^2]}{e} \qquad (52)$$

Finally, the last boundary condition becomes

$$\lim_{r\to a}\tau_{rz}^{(f)} = \begin{cases} \lim_{r\to a}\tau_{rz}^{(m)} \quad ; \quad c < z < \infty & (53a) \\[2mm] \lim_{r\to a}(\mu\sigma_{rr}^{(m)}) \quad ; \quad 0 < z < c & (53b) \end{cases}$$

where

$$\tau_{rz}^{(f)} = \int_0^\infty s^3\{[2(1-v_f)+e]\hat{B}^{(f)} + \hat{A}^{(f)}\}\exp(-s(a-r))\sin(sz)ds \qquad (54)$$

$$\tau_{rz}^{(m)} = -\int_0^\infty s^3\{\hat{A}^{(m)} + [-2(1-v_m)+e_t]\hat{B}^{(m)}\}\exp(-s(r-a))\sin(sz)ds \qquad (55)$$

$$\sigma_{rr}^{(m)} = -\frac{1}{a}\int_0^\infty s^2\{[1+e_t]\hat{A}^{(m)} + [-(1-2v_m)e_t+(sa)^2]\hat{B}^{(m)}\} \qquad (56)$$

$$\times\exp(-s(r-a))\cos(sz)ds$$

It remains, therefore, for us to satisfy the last boundary condition (53), as well as eq. (29). This will ultimately tie the remaining constant in terms of the applied load of the material system.

8

4. The Integral Equation

In order to solve the dual integral equation (53), we first cast it into the form of a Cauchy singular integral equation of the first kind. For this reason, we let at $r = a$

$$\int_0^\infty s^3(sa)\hat{B}^{(m)}\sin(sz)ds = \psi(z) \quad ; 0 < z < c \qquad (57)$$

and

$$\int_0^\infty s^3(sa)\hat{B}^{(m)}\cos(sz)ds = \phi(z) \quad ; 0 < z < c \qquad (58)$$

where ψ represents an odd function of z and ϕ represents an even function of z. Furthermore, the reader may be reminded that, by construction, equation (53a) is automatically satisfied along the interface segment $c < z < \infty$. Thus, it remains for us to satisfy equation (53b) along the interface segment $0 < z < c$. Without going into the mathematical details, equation (53) may now be written as, after some straight forward manipulations,

$$\alpha_1 \int_{-c}^{c} \frac{\{\psi(\xi)-\mu\phi(\xi)\}}{\xi-z}d\xi = f(z) \quad ; \quad 0 < z < \infty \qquad (59)$$

where we have adopted the following definitions :

$$f(z) = 2\tilde{A}_o \in \{f_e(z) + f_o(z)\} \quad , \qquad (60)$$

with

$$f_e(z) = \{\frac{3(1+\mu+2\mu\nu_f)b}{(z^2+b^2)^2} - \frac{4b^3(6+\mu+2\mu\nu_f)}{(z^2+b^2)^3} + \frac{24b^5}{(z^2+b^2)^4}\} \qquad (61)$$

$$f_o(z) = \{\frac{-4+2\nu_f-G}{(z^2+b^2)^2} - \frac{b^2(-16+8\nu_f-4G-12\mu)}{(z^2+b^2)^3} - \frac{24\mu b^4}{(z^2+b^2)^4}\} \quad . \qquad (62)$$

In writing the function f (z), we have made use of the following approximation

$$U(\xi) = -\tilde{A}_o\frac{\partial^2}{\partial\xi^2}\{\frac{\xi}{b^2+\xi^2}\} \qquad (63)$$

with

$$\in = \frac{-4}{\pi}\frac{(1-\nu_f)}{(3-4\nu_f+G)}; \quad \tilde{A}_o = -0.2089\frac{\sqrt{2\pi}\,\Delta_o aG_f}{(1-\nu_f)}; \quad b = 0.0700a \qquad (64abcd)$$

$$\alpha_1 = -\frac{4G(1-\nu_f)}{(3-4\nu_f+G)} \quad .$$

The general solution of the above integral equation is given by

9

$$\psi(z) - \mu\phi(z) = \frac{-1}{\pi^2\alpha_1}\sqrt{\frac{c-z}{c+z}}\int_{-c}^{c}\sqrt{\frac{c+\xi}{c-\xi}}\frac{f(\xi)}{\xi-z}d\xi + \frac{k}{\sqrt{c^2-z^2}}$$ (65)

where k now represents an arbitrary constant and where the integrals are to be evaluated in the Cauchy Principal Value sense. Without going into the tedious mathematical details, the integrals in equation (65) may now be evaluated and the following result is obtained after simplification.

$$\psi(z) - \mu\phi(z) = -\frac{2}{\pi^2}\frac{\epsilon}{\alpha_1}\frac{\hat{A}_o}{\sqrt{c^2-z^2}}\sum_{k=0}^{4}\left\{\frac{d_e^{(k)}}{(z^2+b^2)^k} + \frac{d_o^{(k)}z}{(z^2+b^2)^k}\right\}$$ (66)

where the coefficients $d_e^{(k)}, d_o^{(k)}$, k = 0, 1, 2, 3, 4 are long expressions involving the material constants of the system. Thus, in view of equations (65), (57) and (58), one may now determine explicitly the coefficient $\hat{B}^{(m)}$. In particular,

$$s^3(sa)\hat{B}^{(m)} = -\frac{2}{\pi^2}\frac{\epsilon}{\alpha_1}\tilde{A}_o\sum_{k=0}^{4}\left\{\frac{d_o^{(k)}}{1}\frac{c}{(c^2+b^2)^k}\left[\frac{J_1(sc)}{1} + \frac{kc^2}{(c^2+b^2)}\frac{J_2(sc)}{(sc)} + \ldots\right]\right.$$

$$\left. + \frac{d_e^{(k)}}{\mu}\frac{1}{(c^2+b^2)^k}\left[\frac{J_o(sc)}{1} + \frac{kc^2}{(c^2+b^2)}\frac{J_1(sc)}{(sc)} + \ldots\right]\right\}$$ (67)

Moreover, in view of equations (47) - (49) and (67), the remaining coefficients may now be determined and the displacement and stress fields can be recovered explicitly.

5. The Stress Fields

As it was previously noted, it is now relatively easy to recover the displacement and the stress fields everywhere within the fiber, and within the matrix, region of the material system. Two areas of special interest are worthy of examination, (i) the neighborhood of the point $|z| = c$ and r = a (see Fig. 4), and (ii) the neighborhood of the point $|z| = 0$ and r = a. In this report, we examine the stress field of the former. Suppressing the long and tedious algebraic manipulations, one can show the stresses to be:

stress field at $|z| = c$ and r = a :

$$\tau_{rz}^{(f)} = \sigma_o B_o\sqrt{\frac{c}{2\epsilon}}\left\{\cos(\tfrac{\phi}{2}) + \mu\sin(\tfrac{\phi}{2})\right\}$$ (68)

$$+\sigma_o B_1\sqrt{\frac{c}{2\epsilon}}\sin(\phi)\left\{\cos(\tfrac{3\phi}{2}) + \mu\sin(\tfrac{3\phi}{2})\right\} + O(\epsilon^o)$$

$$\tau_{rz}^{(m)} = \sigma_o B_o\sqrt{\frac{c}{2\epsilon}}\left\{\cos(\tfrac{\phi}{2}) - \mu\sin(\tfrac{\phi}{2})\right\}$$ (69)

$$+\sigma_o B_1\sqrt{\frac{c}{2\epsilon}}\sin(\phi)\left\{\cos(\tfrac{3\phi}{2}) - \mu\sin(\tfrac{3\phi}{2})\right\} + O(\epsilon^o)$$

10

$$\sigma_{rr}^{(m)} = -\sigma_o B_o \sqrt{\frac{c}{2\varepsilon}} \{\mu \cos(\frac{\phi}{2}) + \sin(\frac{\phi}{2})\} \tag{70}$$

$$-\sigma_o B_1 \sqrt{\frac{c}{2\varepsilon}} \sin(\phi)\{\mu \cos(\frac{3\phi}{2}) + \sin(\frac{3\phi}{2})\} + O(\varepsilon^o)$$

$$\sigma_{zz}^{(m)} = -\sigma_{rr}^{(m)} + O(\varepsilon^0) \tag{71}$$

where

$$B_o = \frac{3.032b}{c}\Delta_o\frac{G_f}{\sigma_o}\left\{\frac{\mu(1+2v_f)-(9+\mu+2\mu v_f)(\frac{b}{c})^2+(6-2\mu-4\mu v_f)(\frac{b}{c})^4}{(3-4v_f+G)}\right\}\frac{1}{(1+(\frac{b}{c})^2)^{(7/2)}} \tag{72a}$$

$$B_1 = -\frac{(1-G)}{4(1-v_f)}B_o \tag{72b}$$

Finally, returning to eq (29), we see that the quantity Δ_o may now be related to the applied load σ_o .

6. Conclusions

Without going into the numerical details, it would be of practical interest to examine how well the actual physical boundary condition $\sigma_{zz}^{(f)} = 0$ is satisfied on the plane z = 0. For this reason, we assume

$$\frac{G_f}{G_m} = 10, \mu = 0.5, \frac{c}{a} = 5, v_f = 0.25 \tag{73}$$

and upon defining

$$S = \frac{1}{G_f\Delta_o}\int\{\sigma_{zz}^{(f)} - \sigma_o\}_{z=0}dr \tag{74}$$

one finds that

$$G_f S\Delta_o + \sigma_o r = 0 \quad, \tag{75}$$

or upon solving for Δ_o

$$\Delta_o = -\frac{\sigma_o \ r}{G_f Sa} = 0.629\frac{\sigma_o}{G_f} \quad. \tag{76}$$

In view of the present analysis, the numerical result for the function S is given in Fig. 5. The reader will notice that its profile is a straight line up to approximately r/a =0.65 where by it begins to deviate. This, however, was to be expected for it is the result of our approximation of the function U (see equation (63)) with a single term. Moreover, it may be noted that the function

11

S does not exhibit any oscillations. While this approximation does effect the boundary condition $\sigma_{zz}^{(f)} = 0$ in the neighborhood of the point $r = a$ and $z = 0$, it can be shown that it has no effect the singular term of the stress fields in the vicinity of the crack tip $| z | = c$. In conclusion, the actual boundary condition is seen to be satisfied a lot better than expected.

Returning next to the stress fields, we note that the usual $\frac{1}{\sqrt{r}}$ singular stress behavior, which is characteristic to crack problems, still prevails in the vicinity of the crack tip, i.e. at the interface point $| z | = c$. Furthermore, the unexpected condition

$$\sigma_{rr}^{(m)} + \sigma_{zz}^{(m)} = O(\varepsilon^0) \qquad\qquad (77)$$

also holds, suggesting, therefor, that an increase in the stress $\sigma_{zz}^{(m)}$ is followed by a proportional decrease in the stress $\sigma_{rr}^{(m)}$.

As a practical matter, the analysis will now be used to derive a criterion with which to predict the debonded interface length 2c, as well as the sufficient conditions required to suppress any further development of the interface crack to that of stage three (please see discussion on top of page 2). Moreover, as it was previously noted, we are presently examining the third stage where the fiber crack has now pupped and where the fiber displacement w has been allowed to posses a finite jump. The results will be reported in a follow-up paper in which the effects of a thermal loading have also been included .

7. References

Rosen, B. W., Tensile Failure of Fibrous Composites, AIAA J., 2 (1964) 1985-91.

Hedgepeth,J. M., Stress Concentrations in Filamentary Structures, Nasa TND-882, National Aeronautics and Space Administration, Langley, 1961.

Penado, F. E., and Folias, E. S., The Three-Dimensional Stress Field Around a Cylindrical Inclusion in a Plate of Arbitrary Thickness, Int. J. of Fracture 39,129-146, 1989

Folias, E. S. , On the Stress Singularities at the Intersection of a Cylindrical Inclusion With the Free Surface of a Plate, Int. J. of Fracture 39, 25-34 , 1989.

Pagano, N. J., Effect of Coating/Interface Properties on Microcracking in Brittle Matrix Composites (BMC), presented at the second France/USA Technology Interchange Meeting, San Diego Ca, March 1995

Nicholas, Ted and Ahmad, J., Modeling Fiber Breakage in a Metal- Matrix Composite, Composite Science and Technology 52, 1994
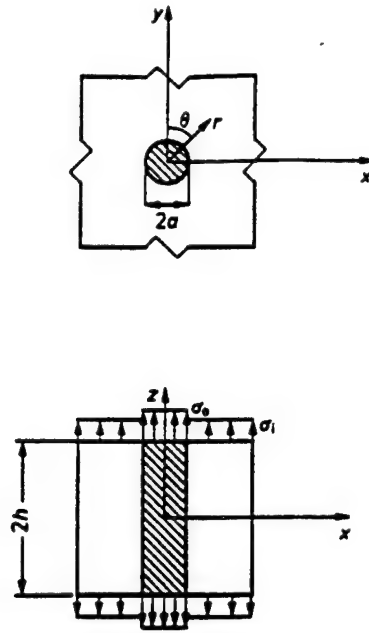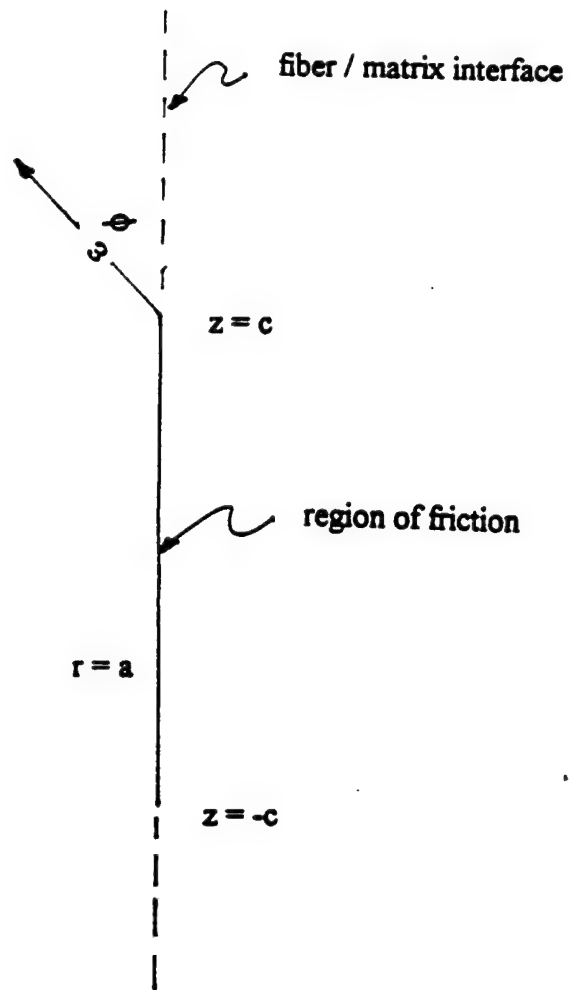
Fig. 1 Geometrical configuration for perfect bonding and no friction at the interface.
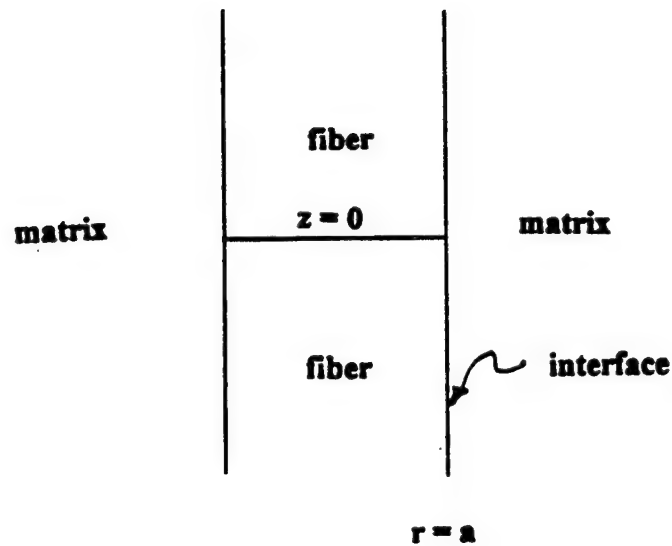
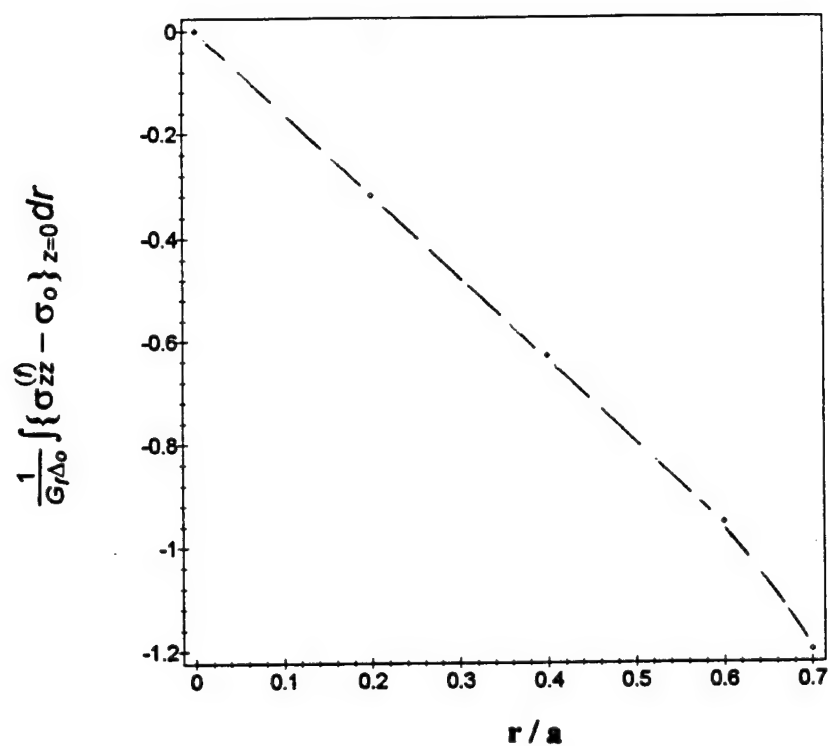**Fig. 2 Geometrical configuration for a cracked fiber with no friction at the interface.**

14
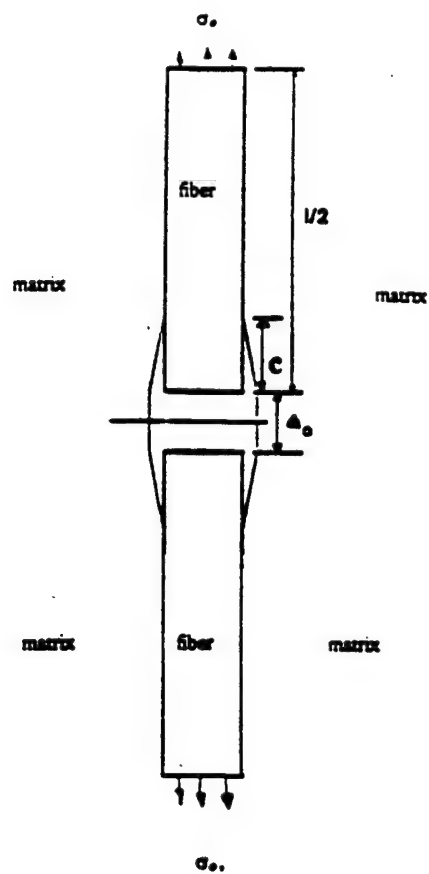
Fig. 3 Geometrical configuration of broken fiber with friction at the interface.

fiber / matrix interface

$z = c$

region of friction

$r = a$

$z = -c$

Fig. 4 Local coordinate system at the point $z = c$.

$$\frac{G_f}{G_m} = 10, \mu = 0.5, \frac{c}{a} = 5, \nu_f = 0.25$$

Fig. 5 Examination of the actual boundary condition $\sigma_{zz}^{(f)}$ on the plane z = 0.

PART II

PREDICTING CRACK INITIATION IN COMPOSITE MATERIAL SYSTEMS DUE TO A THERMAL EXPANSION MISMATCH

by

E. S. Folias

Michael Hohn

ABSTRACT

Residual stresses due to curing and thermal stresses due to differences between the thermal expansion coefficients of the matrix and fiber may have a major effect on the microstresses within a composite material system and must be added to the stresses induced by the external mechanical loads. Such microstresses are often sufficient to produce microcracking even in the absence of external mechanical loads, example during the cooling process.

In this report a few selected results are presented for a material system consisting of SIC-6 cylindrical fibers which are periodically embedded into a plate matrix consisting of beta21 material. The results are based on a linear elastic micromechanics model which provides the stress profiles due to (i) a uniform load perpendicular to the direction of the fibers and (ii) due to a thermal expansion mismatch. In this analysis, perfect bonding between the fiber and the matrix is assumed to prevail. For this case the analysis shows that at a free edge and for a lateral load, there exists a weak stress singularity which increases as the temperature increases. Selected stress profiles are given for the above two loads. Moreover, the application of a fracture criterion shows that no failure is likely to take place for a cooling temperature ΔT of 900^0 C. Thus, the growth of any pre-existing microcracks will be suppressed.

1. INTRODUCTION.

Residual stresses due to curing and thermal stresses due to differences between the thermal expansion coefficients of the matrix and fiber may have a major effect on the micro-stresses within a composite material system and must be added to the stresses induced by the external mechanical loads. Such micro-stresses are often sufficient to produce micro-cracking even in the absence of external loads, example during the cooling process. Furthermore, if the material system is thermally fatigued, these residual stresses may cause some of the existing micro-cracks to grow and coalesce and thus form the presence of larger cracks.

Thus, if rational designs in the use of fiber-reinforced metal matrix composites are to be made, their performance under static, dynamic, and thermally fatigued loads need to be predictable. The first step towards this goal is the realization that the ultimate failure, as well as many other aspects of the composite behavior, are the result of growth and accumulation of microdamage to the fibers, matrix and their interfaces. Thus, it appears that any generally successful model of performance and failure must incorporate the effects of this damage in some way. This certainly represents a challenge. In this paper, we address the form of such damage due to the residual stresses developed as a result of the thermal expansion mismatch between the fibers and the matrix.

In this work, a systematic, 3D, micromechanics approach is used in which the fibers of a composite material system are modeled as cylindrical inclusions that are embedded into a matrix plate. The analytical model is then used to predict, the residual stresses due to a thermal expansion mismatch, e.g. during a cooling process. Moreover, the model provides a better understanding of how the residual stresses are developed and how they can be controlled particularly in relation to ceramics where there is no ductility to accommodate any plastic deformation.

The analysis reveals the dependence of the residual stress field on the fiber volume fraction ratio, identifies the critical locations where a crack is most likely to initiate and subsequently propagate, recovers the interface shear stress profile and provides important information and guidance to material designers for the pre-selection of fiber and matrix materials in order to alleviate some of the residual stresses. It may be noted that the theoretical model is applicable to ceramic and metal/matrix composite systems.

2. MATHEMATICAL MODEL.

Consider in infinite plate matrix which consists of material Beta21, see fig. 1. The matrix plate is assumed to extend to infinity both in the x- and y- directions. In the z-direction, the matrix plate is assumed to have a finite dimension, 2h, in order to capture any possible 3D effects that may be present. A uniform and square periodic set of cylindrical, SIC-6, fibers are embedded into the matrix plate in the directions of both x and y. Two types of loads are being considered : (i) a uniform transverse load σ_o perpendicular to the direction of the fibers and along the y-direction and (ii) a uniform temperature load ΔT (cooling) that is applied throughout the material system. Both fibers and matrix are assumed to be homogeneous and linear elastic.

1
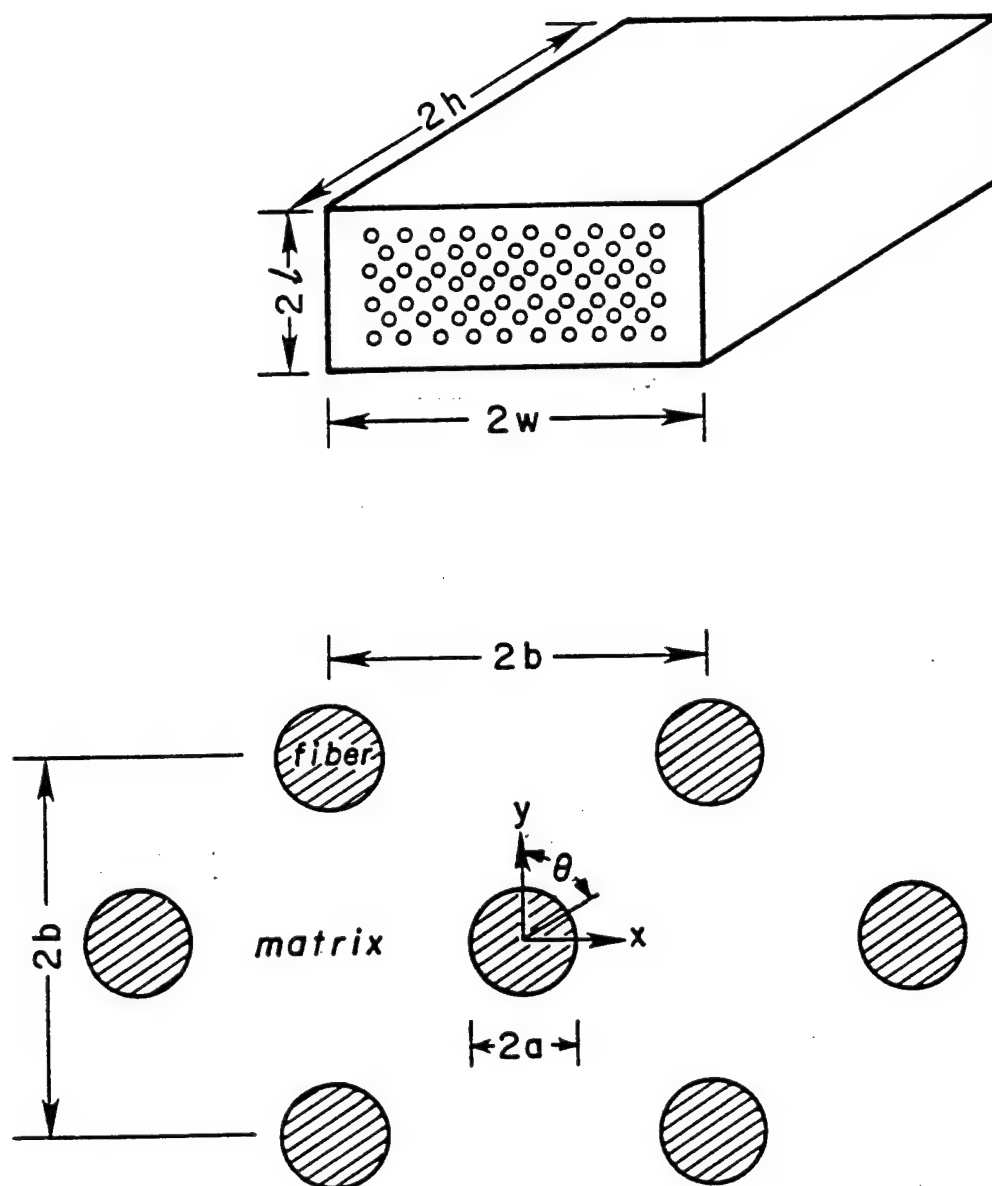
Fig. 1. Geometrical configuration.

The governing equations, are the well known Navier's equations coupled with the Energy Balance equation. More specifically,

$$\frac{1}{1-2v}\frac{\partial u}{\partial x} + \nabla^2 u - \frac{2(1+v)}{1-2v}\frac{\partial T}{\partial x} = 0 \tag{1}$$

$$\frac{1}{1-2v}\frac{\partial v}{\partial y} + \nabla^2 v - \frac{2(1+v)}{1-2v}\frac{\partial T}{\partial y} = 0 \tag{2}$$

$$\frac{1}{1-2v}\frac{\partial w}{\partial z} + \nabla^2 w - \frac{2(1+v)}{1-2v}\frac{\partial T}{\partial z} = 0 \tag{3}$$

$$\nabla^2 T = 0 \tag{4}$$

As to boundary conditions, (i) the appropriate stresses are required to vanish at the free edge, (ii) perfect bonding is assumed to prevail at the fiber / matrix interface, (iii) finally the boundary conditions within the cell configuration are required to be satisfied. Once the displacement field has been completely determined, the stresses can be obtained by using the stress-strain relations:

$$\sigma_{ij} = \lambda \delta_{ij}\varepsilon_{kk} + 2G\varepsilon_{ij} - \alpha(3\lambda + 2G)(T - T_0)\delta_{ij}. \tag{5}$$

3. THE 3D DISPLACEMENT FIELD.

Without going into the mathematical details, the 3D displacement field has been derived by Folias (1976) and can be expressed as :

$$u^{(c)(j)} = \frac{1}{m_j-2}\sum_{v=1}^{\infty}\frac{\partial H_v^{(j)}}{\partial x}\{2(m_j-1)f_1(\beta_v z) + m_j f_2(\beta_v z)\} \tag{6}$$

$$+ \sum_{n=0}^{\infty}\frac{\partial H_v^{(j)}}{\partial y}\cos(\alpha_n h)\cos(\alpha_n z) + I_1^{(j)} - y\frac{\partial I_3^{(j)}}{\partial x} + \frac{1}{m_j+1}z^2\frac{\partial^2 I_3^{(j)}}{\partial x \partial y}$$

$$v^{(c)(j)} = \frac{1}{m_j-2}\sum_{v=1}^{\infty}\frac{\partial H_v^{(j)}}{\partial y}\{2(m_j-1)f_1(\beta_v z) + m_j f_2(\beta_v z)\} \tag{7}$$

$$- \sum_{n=1}^{\infty}\frac{\partial H_n^{(j)}}{\partial x}\cos(\alpha_n h)\cos(\alpha_n z) + \frac{3m_j-1}{m_j+1}I_3^{(j)} + I_2^{(j)} - y\frac{\partial I_3^{(j)}}{\partial y} - \frac{1}{m_j+1}z^2\frac{\partial^2 I_3^{(j)}}{\partial x^2}$$

$$w^{(c)(j)} = \frac{1}{m_j-2}\sum_{v=1}^{\infty}\frac{\partial H_v^{(j)}}{\partial z}\{-2(m_j-1)f_1(\beta_v z) + m_j f_2(\beta_v z)\} - \frac{1}{m_j+1}z\frac{\partial I_3^{(j)}}{\partial y} \tag{8}$$

where,

$$f_1(\beta_v z) = \cos(\beta_v h)\cos(\beta_v z) \tag{9}$$

$$f_2(\beta_v z) = (\beta_v h)\sin(\beta_v h)\cos(\beta_v z) - (\beta_v z)\cos(\beta_v h)\sin(\beta_v z) \tag{10}$$

3

$$\left(\frac{\partial^2}{\partial x^2} + \frac{\partial^2}{\partial y^2} - \beta_\nu^2\right)H_\nu^{(j)} = 0 \tag{11}$$

$$\left(\frac{\partial^2}{\partial x^2} + \frac{\partial^2}{\partial y^2} - \beta_\nu^2\right)H_n^{(j)} = 0. \tag{12}$$

and l_1, l_2, l_3 are 2D harmonic functions. Furthermore, it may be noted that the first series has complex eigenvalues and eigenfunctions while the second has only real eigenvalues and eigenfunctions. For an explicit definition of all functions see Penado and Folias (1989).

4. LOADING TRANSVERSE TO THE FIBERS.

(i) Interior Stress Field:

For a uniform transverse loading along the fiber direction and under the assumption that perfect bonding prevails at the fiber / matrix interface, the 3D stress field (at the interface) and along the fiber length is found to be constant (see Fig. 2) all along the interior and that as one approaches the free surface a boundary layer is noted to prevail where the stress field increases rather rapidly. This rapid change suggests, therefore, the presence of a possible stress singularity. Moreover, the width of this 3D boundary layer is, approximately, two fiber diameters from the free edge. The reader may also note that a second, 3D, effect is that the amplitude of the stresses at the center of the fiber length is, in general, a function of the ratio of fiber diameter / fiber length. If that ratio, however, happens to be less than or equal to 1/10, then all along the interior a 'pseudo plane strain' condition prevails. Figs. 2a, 2b depict the profile of the interface stresses at $\theta=0$ as a function of z / h. The numerical results are specialized for the material system : SCS-6 / fibers, Beta21 / matrix. Figs. 3, and 4, show typical interface stress profiles of the matrix and fiber on the plane z=0, and as functions of the angle θ. The reader may notice that the max. of the stresses occurs at the location $\theta = 0$.

(ii) Edge stress Field:

As it was previously noted, in the neighborhood where one approaches a free surface e.g. the edge of the plate or in the vicinity of crack bridging (see Fig. 5 below), there may very well be present a stress singularity. Utilizing a local, 3D, asymptotic analysis one can substantiate the presence of a weak stress singularity. Complete details of this analysis may be found in the work of Folias (1989). Without going into the mathematical details, a summary of the results, at room temperature and for the composite material system discussed, is given below:

4

NORMALIZED STRESSES AT THE INTERFACE

MATERIAL SYSTEM : SCS-6 / FIBER, BETA21 / MATRIX

LOADING : UNIFORM TENSION TRANSVERSE TO THE FIBER

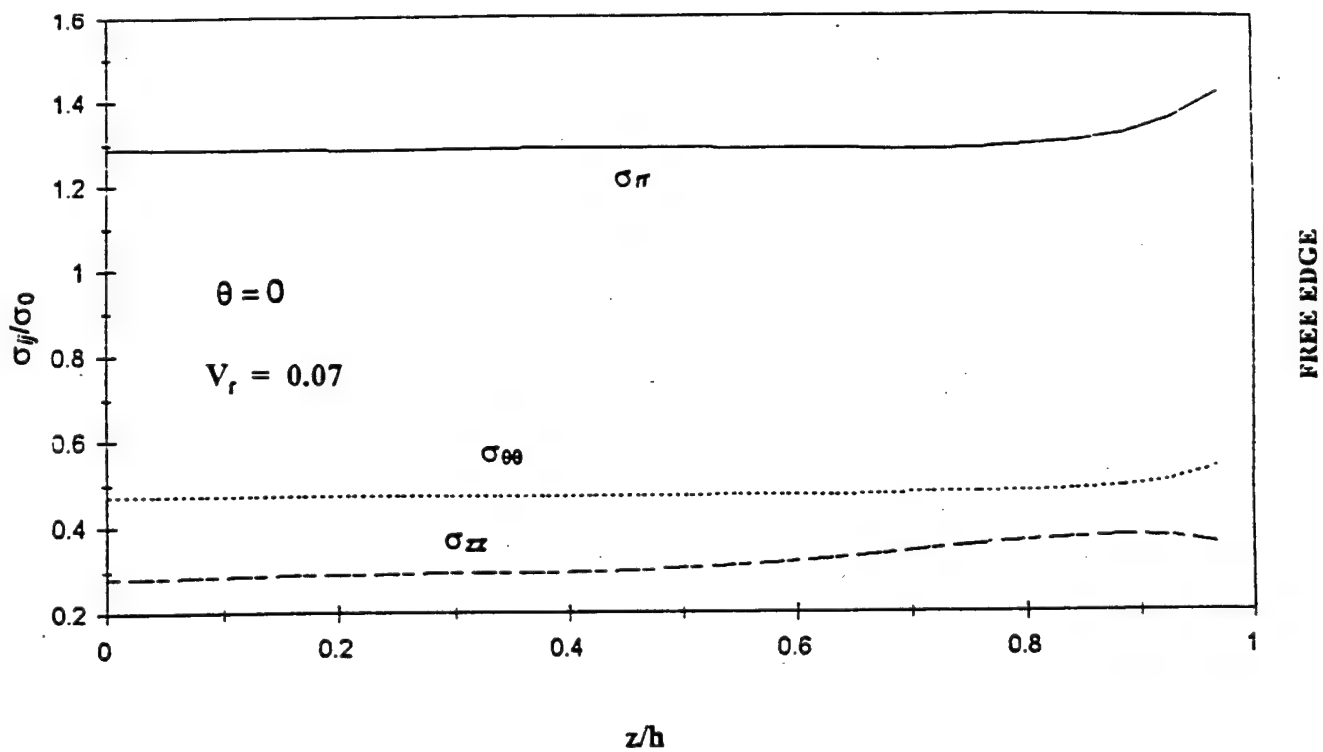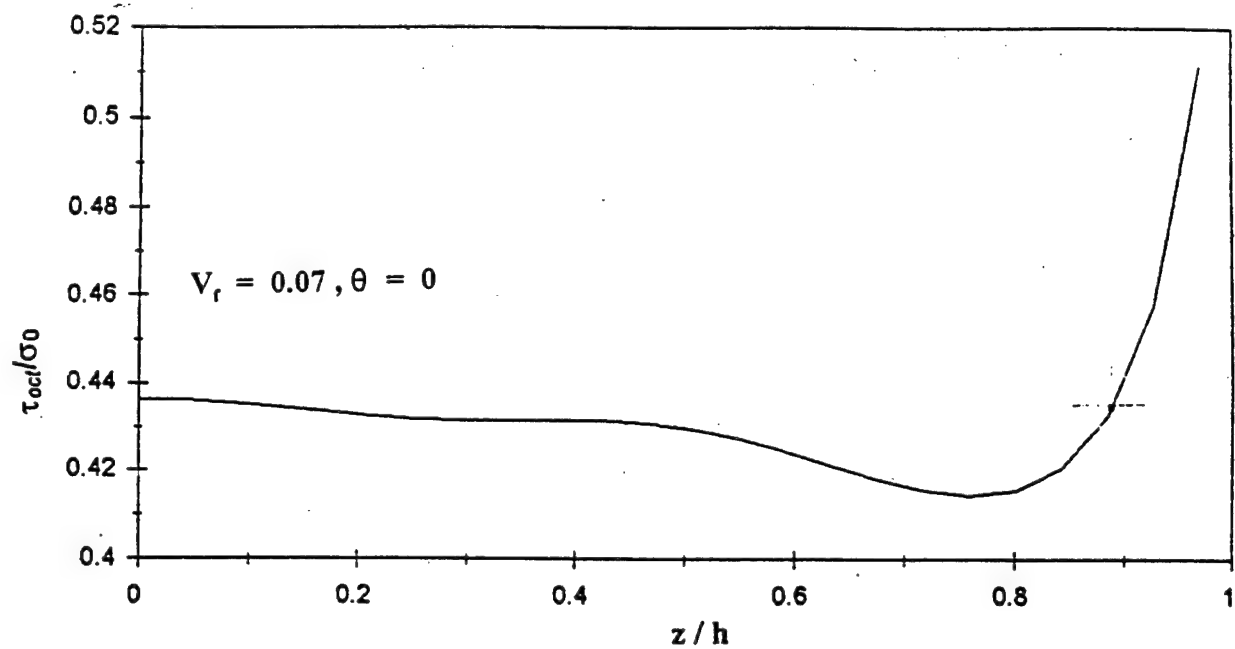FIBER DIAMETER / FIBER LENGTH = 1/10

Fig. 2a. Interface matrix stresses as a function of z/h.

NORMALIZED OCTAHEDRAL SHEAR STRESS AT THE INTERFACE

MATERIAL SYSTEM : SCS-6 / FIBER, BETA21 / MATRIX

LOADING : UNIFORM TENSION TRANSVERSE TO THE FIBER
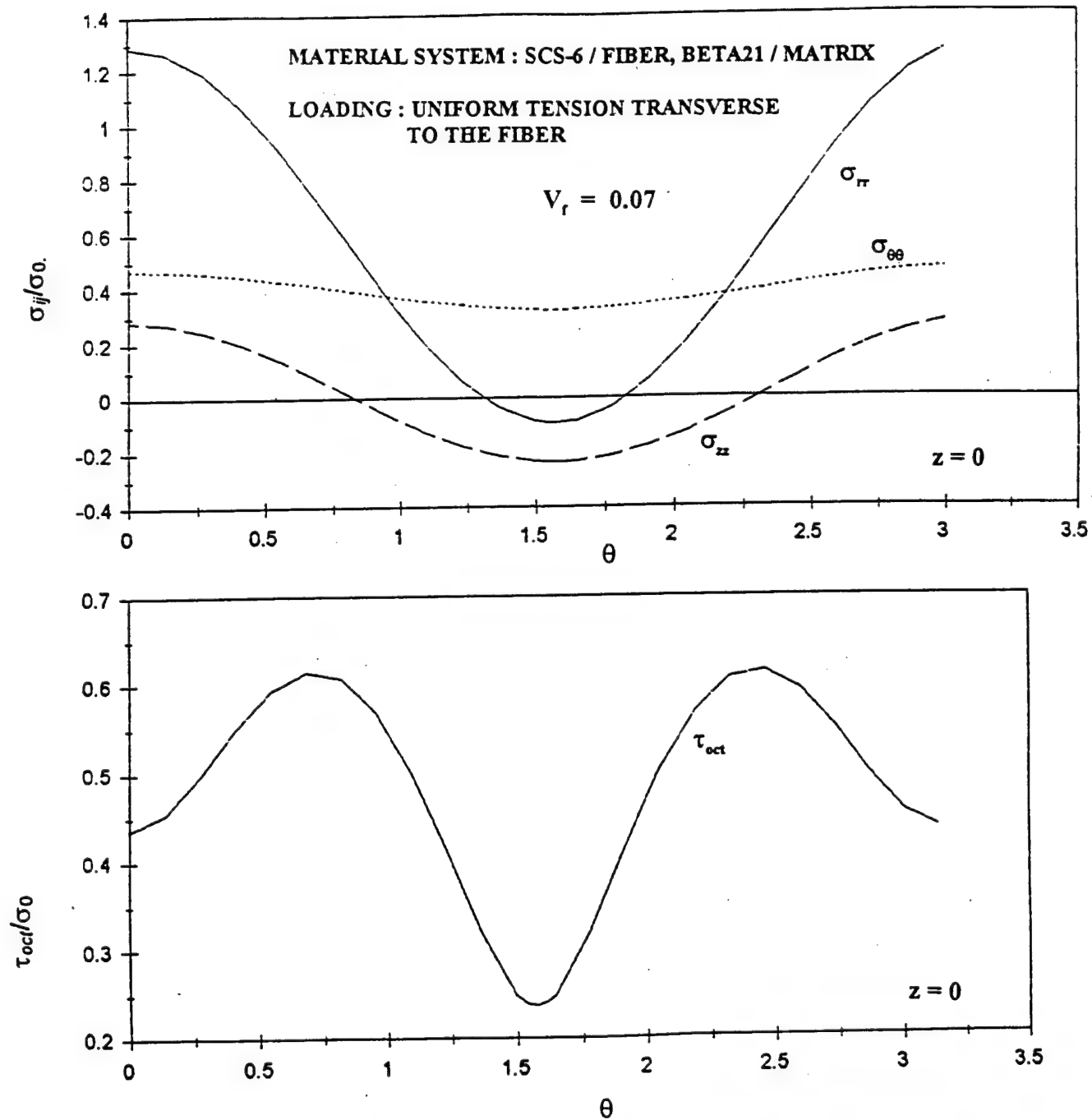
FIBER DIAMETER / FIBER LENGTH = 1/10

Fig. 2b. Interface matrix octahedral shear stress as a function of z/h.

NORMALIZED STRESSES AT THE INTERFACE

MATERIAL SYSTEM : SCS-6 / FIBER, BETA21 / MATRIX

LOADING : UNIFORM TENSION TRANSVERSE TO THE FIBER

FIBER DIAMETER / FIBER LENGTH = 1/10

Fig. 3. Interface matrix stresses on the plane z=0 and as a function of θ.

NORMALIZED STRESSES AT THE INTERFACE

MATERIAL SYSTEM : SCS-6 / FIBER, BETA21 / MATRIX

LOADING : UNIFORM TENSION TRANSVERSE TO THE FIBER

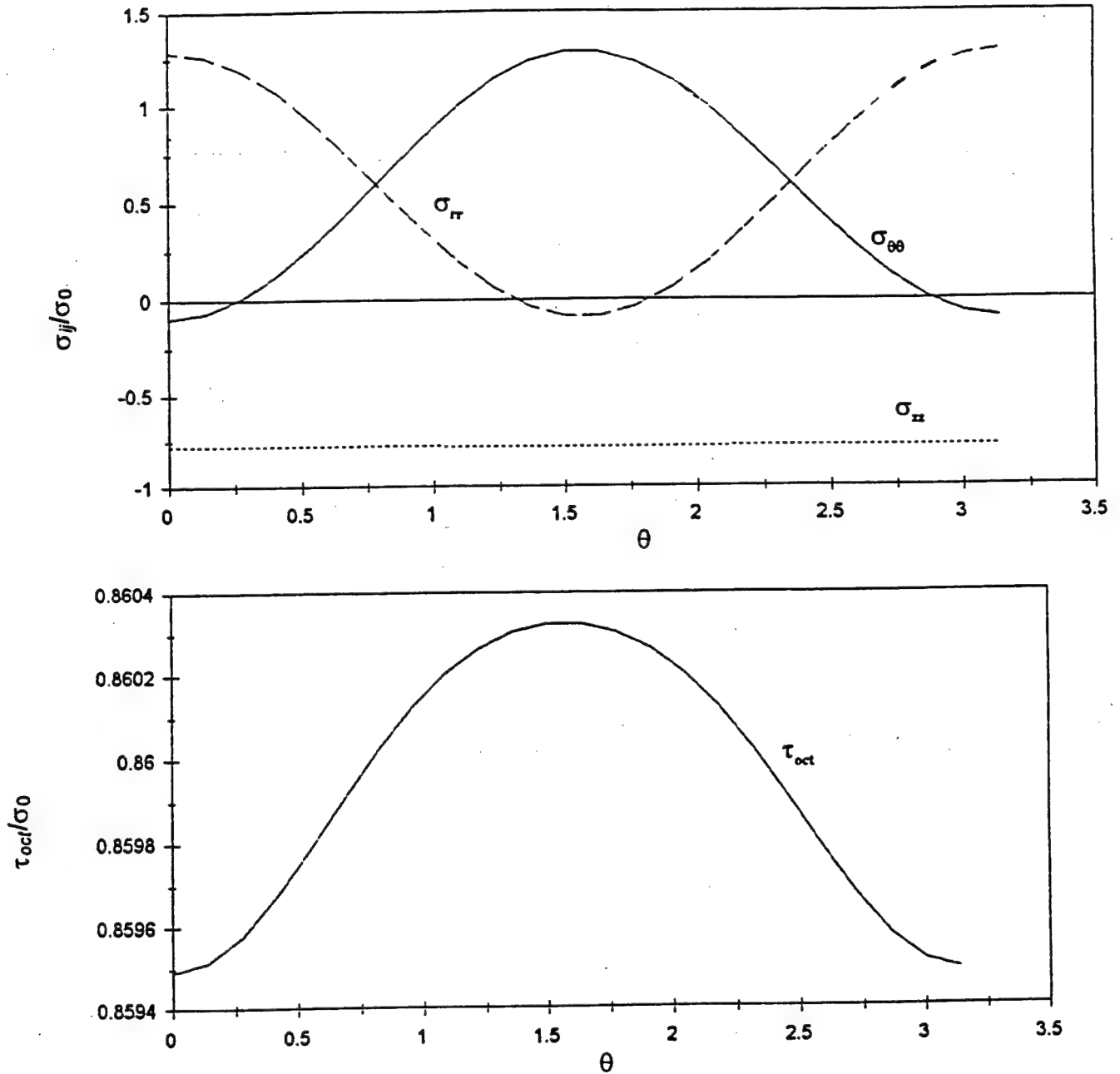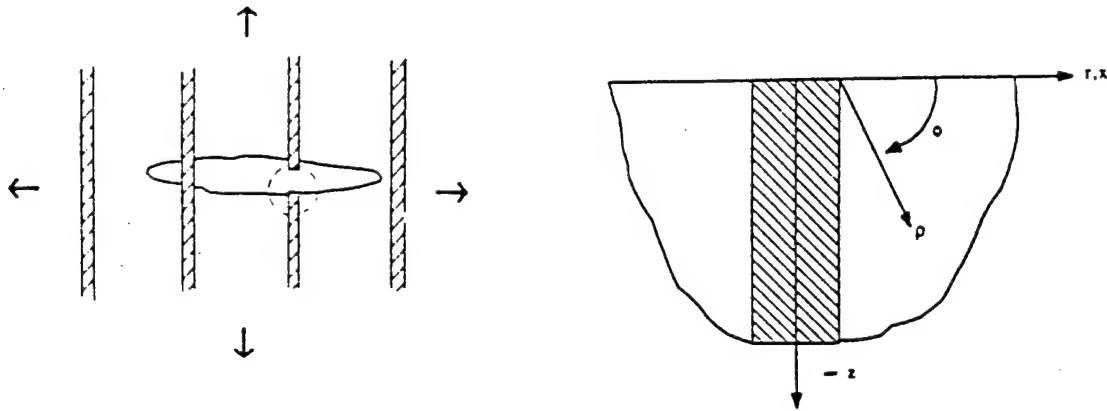FIBER DIAMETER / FIBER LENGTH = 1/10

Fig. 4. Interface fiber stresses on the plane z=0 and as a function of θ.

CORNER ANALYSIS AT THE EDGE

Possible composite failure mode

FIBER MEETING A FREE EDGE

Local 3D Stress Field : (Folias IJF 1989)

$$\sigma_{ij} = \rho^{-\alpha} F_{ij}(\theta, \phi)$$

where for a Titanioum matrix and SiC fibers

$\alpha = 0.110$, **at room temperature**

$\alpha = 0.190$, **at 900^0 C**

(i) **location :** $\phi = \frac{\pi}{2}$, for $G_f/G_m = 3.608$

$$\sigma_{rr}^{(m)} = -11.219\rho^{-\alpha}B^{(f)}$$

$$\sigma_{\theta\theta}^{(m)} = -4.823\rho^{-\alpha}B^{(f)}$$
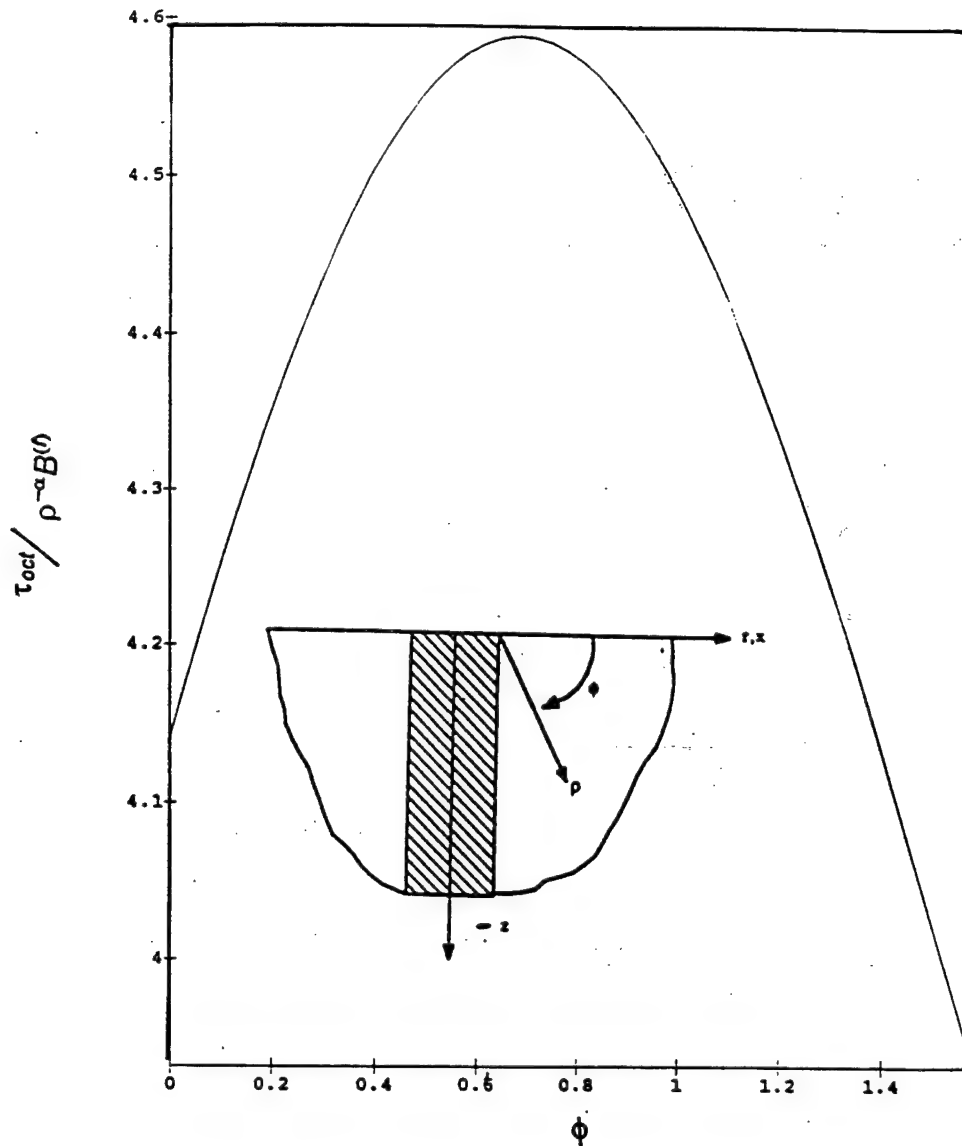
(ii) **location :** $\phi = 0.$

$$\sigma_{rr}^{(m)} = -9.97\rho^{-\alpha}B^{(f)}$$

$$\sigma_{\theta\theta}^{(m)} = -3.391\rho^{-\alpha}B^{(m)}.$$

Fig. 5. Geometrical configuration and basic results.

9

OCTAHEDRAL SHEAR STRESS AT THE CORNER OF A FREE EDGE:

The max. octahedral shear stress for $G_f/G_m = 3.608$ occurs at $\theta = 40^0$.

REMARK : Crack will initiate at the fiber edge and at the interface and will then follow the direction of the max. octahedral shear stress.

Fig. 5b. The octahedral shear stress at the corner.

10

The following observations are worthy of note. First, as the ratio of the shear moduli increases, so is the stress singularity. This is compatible with our physical expectations and within the assumptions of our theory. Second, all things being equal, at the edge the controlling stress for failure is the radial stress particularly at the location $\phi=0$ and $\theta=0$.

	Room Temp.	**900° C**
at $\phi = 0$:	$\sigma_{rr}^{(m)}/\sigma_{\theta\theta}^{(m)} = 2.94$	$\sigma_{rr}^{(m)}/\sigma_{\theta\theta}^{(m)} = 2.94$
at $\phi = \pi/2$:	$\sigma_{rr}^{(m)}/\sigma_{\theta\theta}^{(m)} = 2.33$	$\sigma_{rr}^{(m)}/\sigma_{\theta\theta}^{(m)} = 2.18$

Similarly, in the vicinity of the edge, the octahedral shear stress attains a maximum at an angle $\phi=40$ degrees (see Fig. 6). It is interesting to note that in this neighborhood, the ratio of

$$\tau_{octmax}|roomtemp/\tau_{octmax}|900°C = 1/2.09$$

This suggests, therefore, that as ΔT increases the application of a transverse loading will cause the matrix to undergo substantial more plastic deformation in this region.

Computing next the displacement at the free surface $z = h$, we notice that its magnitude increases at elevated temperatures.

$$w|_{\phi=0,\theta=0,RoomTemp}/w|_{\phi=0,\theta=0,900°C} = 1/1.6.$$

Physically, this suggests that a mode I, II and III crack failure will initiate at the edge and at the interface due to an applied load transverse to the fibers.

5. RESIDUAL STRESSES DUE TO A THERMAL LOAD.

Residual stresses due to curing and thermal stresses due to differences between the thermal expansion coefficients of the matrix and fiber may have a major effect on the microstresses within a composite material system and must be added to the stresses induced by the external mechanical loads. Such microstresses are often sufficient to produce microcracking even in the absence of external loads, example during the cooling process.

In this investigation, a systematic, 3D, micromechanics approach is used in which the fibers of a composite material system are modeled as cylindrical inclusions which are embedded into a matrix plate. The analytical model is then used to predict, the residual stresses due to a thermal expansion mismatch, eg. during the cooling process. Moreover, the model provides a better understanding of how the residual stresses are developed and how they can be controlled particularly in relation to ceramics where there is no ductility to accommodate plastic deformation.

The analysis reveals the dependence of the residual stress field on the fiber volume fraction ratio, identifies the critical locations where a crack is most likely to initiate, recovers the interface shear stress profile and provides important information to the material designers for the pre-selection of fiber and matrix materials in order to alleviate some of the residual stresses.

Without going into the mathematical details, we consider a composite material system consisting of SIC-6 fibers which are embedded into a beta21 matrix plate and the entire system is then exposed to an environment of a uniform cooling temperature ΔT. While it is true that the material constants do change as a function of the temperature, the thermal coefficients appear in the solution as a ratio and interestingly enough this ratio changes vary little. On the other hand, the ratio of the shear moduli changes considerably as the temperature varies. Thus, the results are very much dependent on the material properties which one uses. Thus, if one bases the analysis on the shear moduli ratio at room temperature, the following stress profiles are recovered at the fiber / matrix interface. Fig. 7 depicts the radial matrix stress on the plane z=0 and as a function of the angle θ. It is noted that the radial stress is compressive. Similarly, the tangential stress is tensile in nature and its maximum occurs at the location of $\theta = 0$. In general, the location of this maximum is a function of the material properties and particularly the shear moduli ratio. Moreover, in the above analysis perfect bonding was assumed to prevail at the fiber / matrix interface. If, however, we relax the conditions at the interface and allow slippage then the maximum occurs elsewhere. More specifically in this case it occurs at $\theta = 45$.

Examining next the possibility of matrix cracking, it becomes evident from the above that no cracking will occur in the matrix for a $\Delta T = 900^{\circ}C$. This matrix material is too strong for preexisting microcracks to grow. Examination of the σ_{zz} stress also shows that no cracks will develop in that direction either. These results are in line with the obtained in house results based on finite elements (J. Kroupa, 1994).
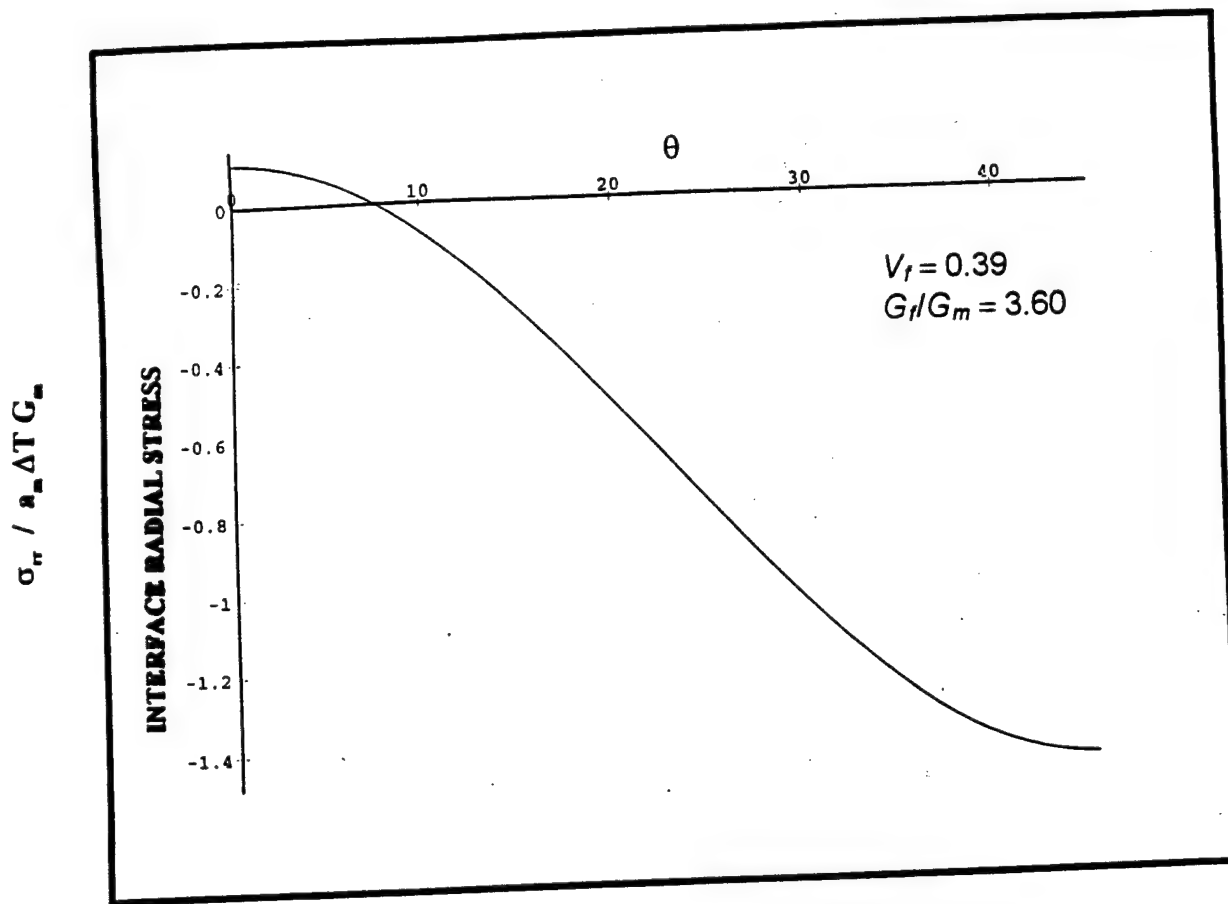
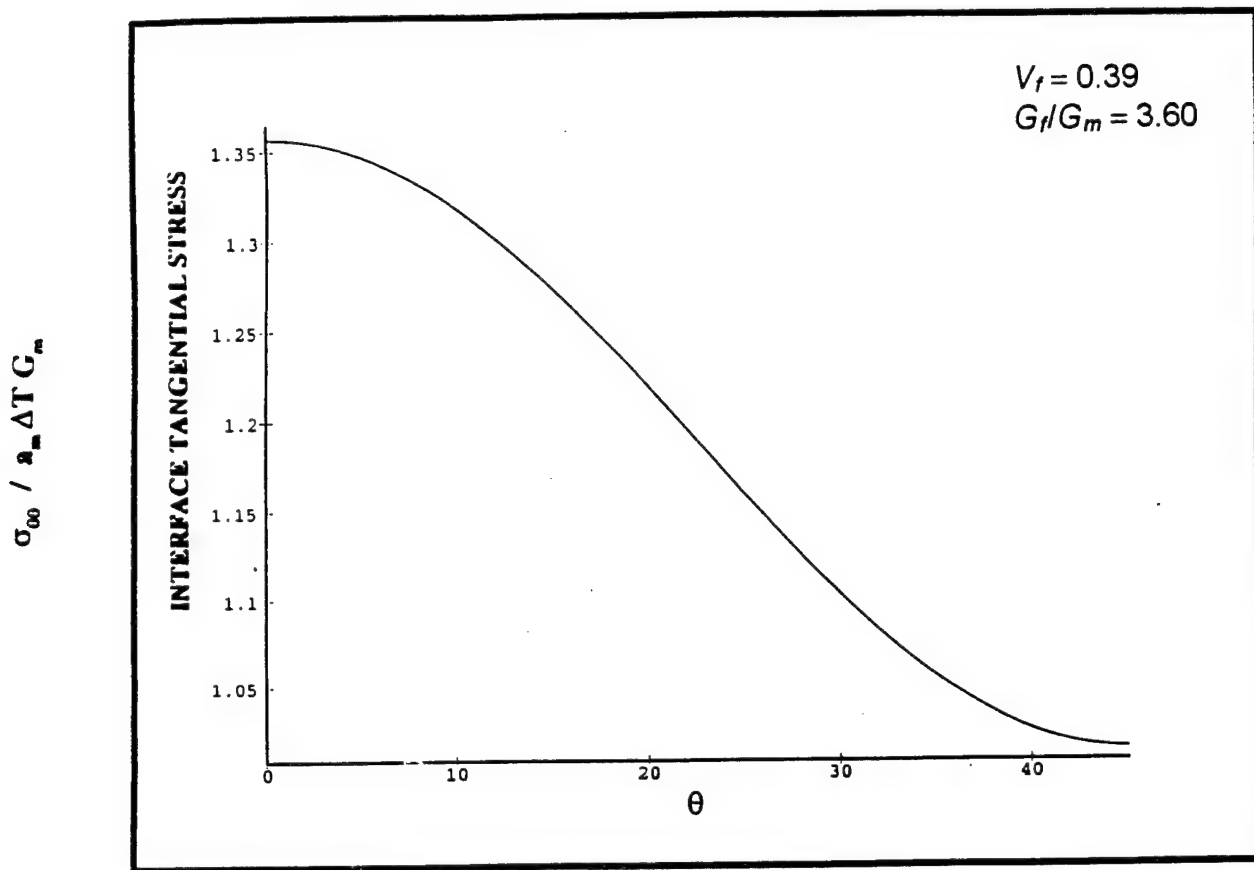Fig. 7. Interface radial matrix stress on the plane z=0 and as a function of θ.

Fig. 8. Intêrface $\sigma_{\theta\theta}$ matrix stress on the plane z=0 and as a function of θ.

Finally, it should be noted that the effect of the shear moduli ratio on the interface stresses is substantial. This can be seen by the following comparison of the tangential interface stress when using three different shear modulii ratios which reflect different temperature levels:

V_f	$\sigma_{\theta\theta}/(\alpha_m G_m \Delta T)$ Room Temp.	$\sigma_{\theta\theta}/(\alpha_m G_m \Delta T)$ Mid Temp.	$\sigma_{\theta\theta}/(\alpha_m G_m \Delta T)$ HighTemp.
0.39	1.36	1.59	1.64

Although it would be desirable to have a program in which the material properties do vary with temperature, one can compensate by taking the results corresponding to the high shear modulii ratio. The thermal expension coefficients on the other hand appears as a ratio which ratio does not vary appreciably to make any significant differences.

The variation of the normalized tangential interface stress as a function of the fiber volume fraction, for this material, is almost linear and may be approximated with the equation

$$\frac{\sigma_{\theta\theta}}{\alpha_m G_m \Delta T} = 0.92 + 1.02 V_f + 0.28 \quad V_f^2. \tag{13}$$

6. CONCLUSIONS.

In view of the above, the matrix will not exhibit any cracking as a result of the residual stresses which are developed during the cooling process ($\Delta T = 900^0 C$). Moreover, the residual stresses predicted are in very good agreement with those obtained in house. (WL/MLLN)

7. REFERENCES.

Folias, E. S. Jof A. M., 1976.

Penado, E. and Folias, E. S., IJofF,1989.

Folias, E. S., and Hohn, M., Private communication.

Kroupa, J., private communication.

15

PART III

Partial Debonding at a Fiber/Matrix Interface
A NOVEL NUMERICAL APPROACH

by
Michael Hohn
E.S. Folias

November 15, 1996

1 Introduction

In design, anticipation of material failure is vital. Over the last decades, a theory first proposed by Griffith has become one of the most used tools in prediction of fracture of simple materials. In the Griffith theory, a material is assumed to have microscopic cracks with high stresses found at their tips; these cracks cause the material to fail at a much lower level than molecular binding forces predict. To accurately predict failure of these materials requires knowledge of the stress field near the tips.

Composite materials also have cracks, but models are much more involved because of material interactions. As before, accurate determination of the stress field, especially near high stress regions, is vital for failure prediction.

For all but the simplest geometries, closed form solutions are almost impossible to obtain, so numerical methods have become very popular. For material science, by far the most popular methods are the finite element (FE) methods. Some of their desirable properties are relative conceptual simplicity, straightforward (but tedious) implementation, a large available code base for solving problems, and a tendency to require only modest computing resources. Since finite elements are based on polynomials, the solutions to problems for which finite elements are used must be expressible as a sum of polynomials, or the FE approximation will be very poor. Since functions with unbounded derivatives (i.e. stresses near cracks and material interfaces) cannot be approximated well with polynomials, it is common to use special elements for these functions.

For example, in 2 dimensional problems and some special 3 dimensional cases, it has been shown that the stresses near the crack tips are proportional to $1/\sqrt{r}$, and that the constant of proportionality, K_c, depends only on the geometry of the material. This is enough information to complement the (polynomial based) FE methods with singular elements (which behave like $1/\sqrt{r}$ in the appropriate regions), thus reducing the problem to one for which FE are well suited, and get good numerical answers.

For other 3 dimensional crack problems however, asymptotic expansions have shown the stress fields to be proportional to $r^{-\alpha}$, $0 < \alpha < 1/2$, α depending on the geometry of the material. Thus, for 3D problems, one does not in general know the behavior of the singularity a priori, and the problem cannot be reduced to one which FE can handle well, resulting in low accuracy near singularities. Notice the difficulty here: the stress distribution in the vicinity of a crack also depends strongly on material geometry, making it impossible to separate behavior near cracks from the rest of the material— but this separation is how FE methods handle these problems.

This inherent weakness of most numerical methods — the inability to handle singularities without "assistance" — is not shared by the group of *sinc-*

function based methods. Further, *sinc* methods enjoy an exponential convergence rate, enabling one to get many digits of accuracy with reasonable work, if desired.

For crack and related problems, this means only the *location*, but not the type, of the singularity is needed, and the solution can be accurately computed.

The weakness of using these methods lie in the fact that their use for differential and integral equations is recent, so no large code base yet exists; their use has been largely in 1D problems; and they are not as intuitive as FE or finite difference methods, hence overlooked by most people.

The purpose of this work over the last years has thus been the further development of *sinc* methods for systematic solution of problems in mechanics that possess singularities. The development of the method has been guided by a representative problem, described in detail below.

It should be emphasized that the following problem is only one example of an entire class of problems, serving here to illustrate the effectiveness and flexibility of the *sinc* methods for that class of problems.

It should also be noted that this method is readily extended to handle fully nonlinear material behavior.

The details of the method and development to date comprise the bulk of the remainder of this report.

2 Problem and Solution Approach

The problem here is to find the stress field uniformly to a desired accuracy[1] in the piece of composite material shown in figure 1. To this end, we solve the full isotropic Navier's equations

$$\nabla^2 \mathbf{u} + \frac{1}{1 - 2\nu} \nabla(\nabla \cdot \mathbf{u}) = 0 \tag{1}$$

with appropriate displacement and stress boundary conditions.

This problem is broken down as follows.

1. Using this problem's radial symmetry allows immediate reduction to a sequence of 2D problems on domains as shown in figure 2 — section 2.1.

2. At points $A_1, \ldots, A_4$, singularities are to be expected. Typically, these singularities' behavior depends on approach direction, so each of these problems is further divided into triangles, and these triangles are mapped to coupled rectangles as shown in figures 3 and 4 — section 2.2.

---

[1]Uniform accuracy of 3 digits in both displacements and stresses is easily achieved.

Figure 1: The domain for the full 3D problem. The debonded region is treated as a very thin crack.

Fibrous inclusion

Matrix

Region of debonding
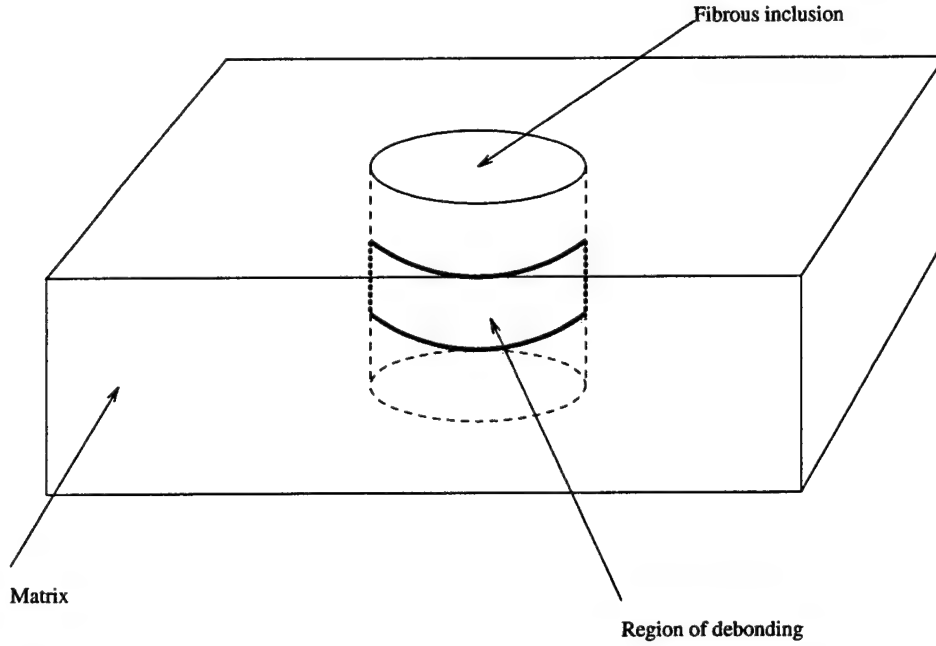
3. The *sinc* method is applied to the resulting collection of rectangles, and the solution is thus obtained — section 2.3.

The details of steps (1) and (2) are currently being worked on, and are progressing rapidly. We therefore only present an outline of the required steps in sections 2.1 and 2.2. The *sinc* method and its application to (3) are found in section 2.3.

2.1 Forming of the 2D sequences

Although the *sinc* methods can be used directly for 3D problems, incremental development is best done for 2D problems first. For the given problem, we take advantage of the geometry and use the substitutions

$$u_r(r, \theta, z) = u_{r,0}(r, z) + \sum_{n=1}^{\infty} u_{r,n}(r, z) \cos\left(\frac{n\theta}{2}\right) \tag{2}$$

$$u_\theta(r, \theta, z) = \sum_{n=1}^{\infty} u_{\theta,n}(r, z) \sin\left(\frac{n\theta}{2}\right) \tag{3}$$

$$u_z(r, \theta, z) = u_{z,0}(r, z) + \sum_{n=1}^{\infty} u_{z,n}(r, z) \cos\left(\frac{n\theta}{2}\right) \tag{4}$$
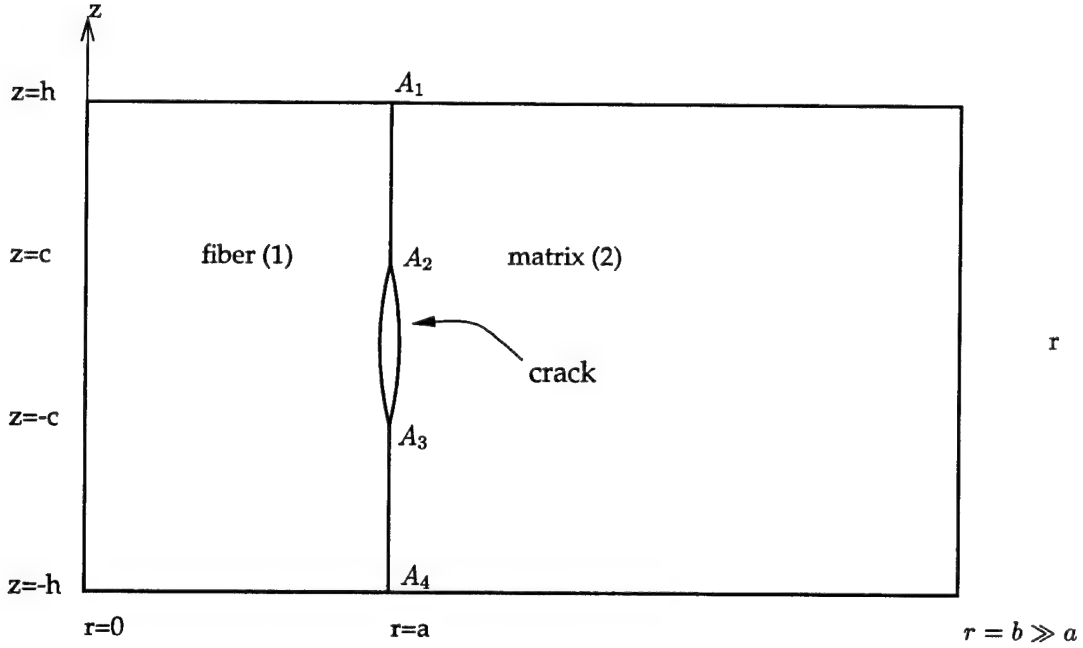
3

Figure 2: Reduced 3D problem. Crack and points with singularities are indicated.

in the polar form of equation 1 to reduce the original equations to the mentioned sequence of 2D problems. The equations governing figure 2 are thus

$$
-2 \left(\frac{\partial^2}{\partial r^2} u_{r,0} \right) \nu + 2 \left(\frac{\partial^2}{\partial r^2} u_{r,0} \right) - 2 \frac{\nu \left(\frac{\partial}{\partial r} u_{r,0} \right)}{r} + 2 \frac{\frac{\partial}{\partial r} u_{r,0}}{r} + \left(\frac{\partial^2}{\partial z^2} u_{r,0} \right)
$$

$$
- 2 \left(\frac{\partial^2}{\partial z^2} u_{r,0} \right) \nu + 2 \frac{\nu \, u_{r,0}}{r^2} - 2 \frac{u_{r,0}}{r^2} + \left(\frac{\partial^2}{\partial z \, \partial r} u_{z,0} \right) = 0 \qquad (5)
$$

$$
\left(\frac{\partial^2}{\partial r^2} u_{z,0} \right) - 2 \left(\frac{\partial^2}{\partial r^2} u_{z,0} \right) \nu + \frac{\frac{\partial}{\partial r} u_{z,0}}{r} - 2 \frac{\left(\frac{\partial}{\partial r} u_{z,0} \right) \nu}{r} + \frac{\frac{\partial}{\partial z} u_{r,0}}{r}
$$

$$
- 2 \left(\frac{\partial^2}{\partial z^2} u_{z,0} \right) \nu + 2 \left(\frac{\partial^2}{\partial z^2} u_{z,0} \right) + \left(\frac{\partial^2}{\partial z \, \partial r} u_{r,0} \right) = 0 \qquad (6)
$$

for the non-θ terms of equations 2–4 and

$$
-2 \left(\nu - 1 \right) \left(\frac{\partial^2}{\partial r^2} u_{r,n} \right) + \frac{1}{2} \frac{\left(-3 + 4 \nu \right) u_{\theta,n} \, n}{r^2} - \left(-1 + 2 \nu \right) \left(\frac{\partial^2}{\partial z^2} u_{r,n} \right)
$$

$$
- 2 \frac{\left(\nu - 1 \right) \left(\frac{\partial}{\partial r} u_{r,n} \right)}{r} - 2 \frac{u_{r,n}}{r^2} + \frac{1}{4} \frac{\left(-1 + 2 \nu \right) u_{r,n} \, n^2}{r^2} + 2 \frac{\nu \, u_{r,n}}{r^2}
$$

$$
+ \left(\frac{\partial^2}{\partial z \, \partial r} u_{z,n} \right) + \frac{1}{2} \frac{\left(\frac{\partial}{\partial r} u_{\theta,n} \right) n}{r} = 0 \qquad (7)
$$

4

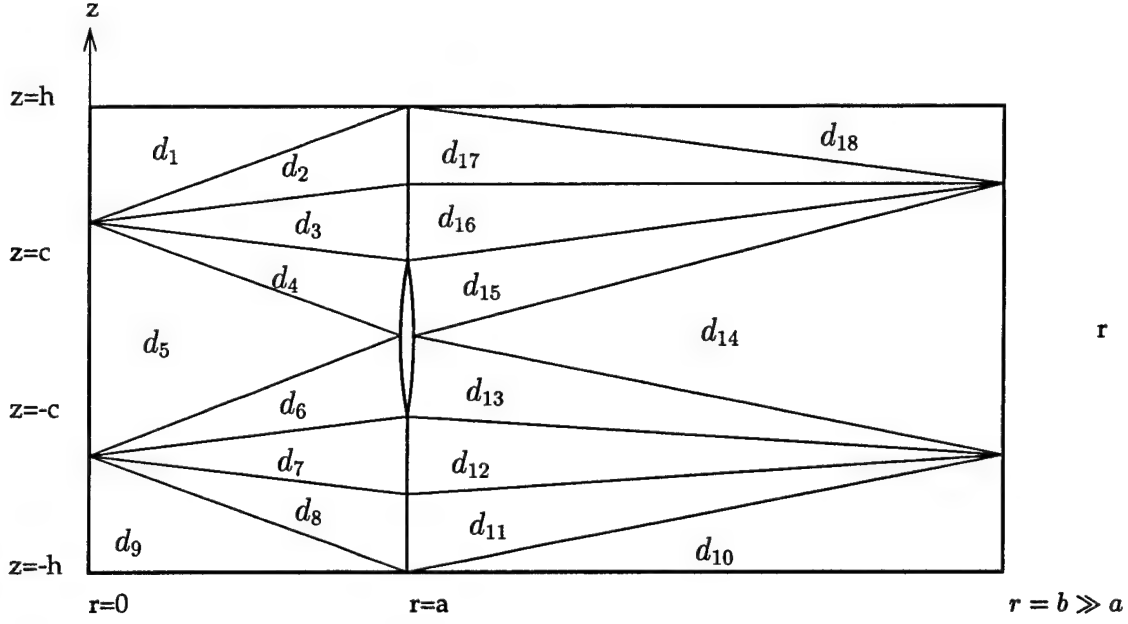Figure 3: Triangulation of reduced problem.

$$
-\frac{(-1+2\nu)\left(\frac{\partial^2}{\partial r^2}u_{\theta,n}\right)}{r} - \frac{(-1+2\nu)\left(\frac{\partial}{\partial r}u_{\theta,n}\right)}{r^2}
$$

$$
+\frac{1}{2}\frac{(\nu-1)u_{\theta,n}n^2}{r^3} + \frac{1}{2}\frac{(-3+4\nu)u_{r,n}n}{r^3}
$$

$$
-\frac{(-1+2\nu)\left(\frac{\partial^2}{\partial z^2}u_{\theta,n}\right)}{r} - \frac{1}{2}\frac{\left(\frac{\partial}{\partial r}u_{r,n}\right)n}{r^2} + 2\frac{\nu u_{\theta,n}}{r^3}
$$

$$
-\frac{u_{\theta,n}}{r^3} - \frac{1}{2}\frac{\left(\frac{\partial}{\partial z}u_{z,n}\right)n}{r^2} = 0 \tag{8}
$$

$$
-2(\nu-1)\left(\frac{\partial^2}{\partial z^2}u_{z,n}\right) - (-1+2\nu)\left(\frac{\partial^2}{\partial r^2}u_{z,n}\right) + \frac{1}{4}\frac{(-1+2\nu)u_{z,n}n^2}{r^2}
$$

$$
+\left(\frac{\partial^2}{\partial z\,\partial r}u_{r,n}\right) + \frac{1}{2}\frac{\left(\frac{\partial}{\partial z}u_{\theta,n}\right)n}{r} - \frac{(-1+2\nu)\left(\frac{\partial}{\partial r}u_{z,n}\right)}{r} + \frac{\frac{\partial}{\partial z}u_{r,n}}{r}
$$

$$
= 0 \tag{9}
$$

for the θ terms – notice the n dependence here.

So far, we thus have one 2 unknown system, and one 3 unknown system, both independent of θ. Of course, each set occurs twice — once for the matrix and once for the fiber, and appropriate coupling is done across the boundaries by matching stresses and displacements above and below the crack, and requiring zero stresses at the crack.

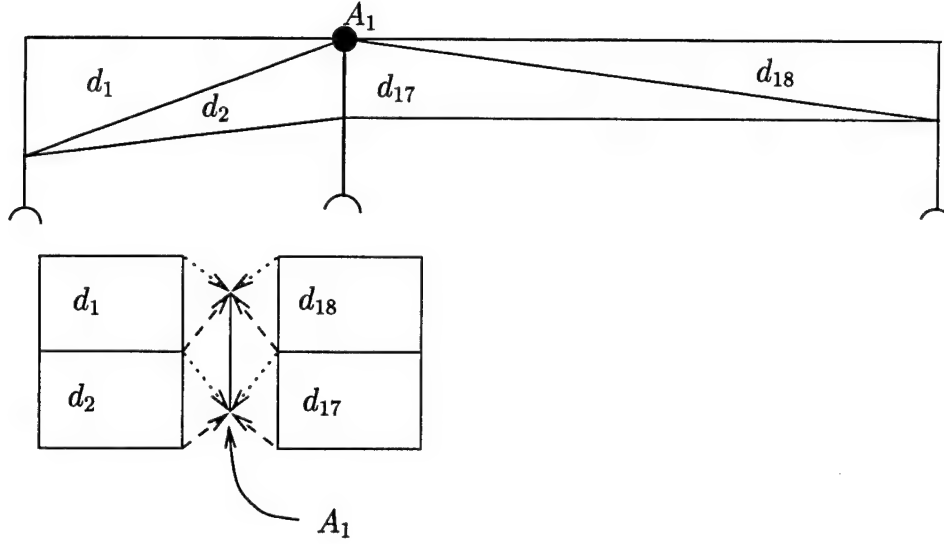The boundary conditions are transformed similarly.

5

Figure 4: Rectangular solution regions from triangulation of reduced problem. Notice that the four domains shown share the boundary that came from the point A_1

2.2 Mapping of the Triangulation

After the reduction to a sequence, there may be singularities at the points $A_1, \ldots, A_4$ (figure 3). Most likely, these will be *moving singularities*, e.g. using a second polar coordinate system with origin at point A_1, the displacements may have a form similar to $f = r^\alpha \sin(\theta)$, $0 < \alpha < 1/2$. In the coordinate system used in figure 2, f would behave like $z(r^2 + z^2)^{\alpha/2-1/2}$ near A_1, and its partials would have the dominant term $rz/(r^2 + z^2)^{3/2-\alpha/2}$. This form of singularity is easily changed to a more suitable form via the mappings $r = \xi$, $z = \eta\xi$. Geometrically, this means splitting rectangular domains into triangular pieces, as shown in figure 3. Algebraically, this mapping turns dominant terms of derivatives into the form $1/\xi^{1-\alpha}$, which no longer depends on approach direction, enabling direct solution using *sinc* methods.

2.3 Sinc Method Description

It is the purpose of this chapter to give necessary background for the understanding of *sinc* methods as used for the present work. We begin with some known one-dimensional results in section 2.3.1; the extension to two dimensions is shown in section 2.3.2. The extension to higher dimensions is similar, and will not be shown here.

Section 2.3.2.5 demonstrates a 2 dimensional, multiple unknown, multiple-domain problem of the type occurring after the triangulation done above.

6

2.3.1 Sinc methods for 1D problems

In this section, we summarize some available results for *sinc* interpolation and *sinc* collocation. The main reference for technical details of this section is the book *Numerical Methods based on Sinc and Analytic Functions*, Springer, 1993; most results are proven there.

2.3.1.1 Interpolation and simple collocation First, some definitions.

The *sinc* (or Whittaker Cardinal) function is defined by

$$\text{sinc}(x) = \frac{\sin(\pi x)}{\pi x} \tag{10}$$

Define the domain D_d by

$$D_d = \{w \in C | \Im(w) < d\} \tag{11}$$

Let $\alpha > 0$, and let $L_\alpha(D_d)$ denote the family of functions f with the properties

- f is analytic in D_d;

- for some $c > 0$ and all $z \in D_d$,

$$|f(z)| \leq c \frac{e^{\alpha z}}{(1 + |e^z|)^{2\alpha}} \tag{12}$$

Now, taking $h = \left(\frac{\pi d}{\alpha N}\right)^{1/2}$, we have the interpolation result

$$f(x) = \sum_{k=-N}^{N} f(kh) \, \text{sinc}\left(\frac{x - kh}{h}\right) + E(N)$$

$$E(N) = c_1 \sqrt{N} e^{-\sqrt{\pi d \alpha N}} \tag{13}$$

for a positive c_1 depending only on f, d and α. Notice that this result is for the real line, and the function must decay at $\pm\infty$.

By first remapping functions approaching a nonzero limit, this can be enhanced to handle non-zero values at $\pm\infty$:

$$f(x) = \sum_{k=-M}^{N} c_k \, \text{sinc}\left(\frac{x - kh}{h}\right) + c_{N+1} S_\infty(x) + c_{-M-1} S_{-\infty}(x) + E(N) \tag{14}$$

$$c_k = f(kh), \; k = -N..N \tag{15}$$

$$c_{-M-1} = f(-\infty) \tag{16}$$

$$c_{N+1} = f(\infty) \tag{17}$$

$$S_{-\infty}(x) = \frac{1}{1 + e^{\alpha x}} \tag{18}$$

$$S_\infty(x) = \frac{e^{\alpha x}}{1 + e^{\alpha x}} \tag{19}$$

7

Notice that the summation runs from $-M$ to N; the error bound is of the same form as above.

Defining m as $m = 2N+1$, this means once n digits of accuracy are obtained, one can roughly get $1.4n$ digits by doubling m.

To interpolate a function f defined on $[a, b] \subset \mathbf{R}$ we first make the following definitions:

1. for $[a, b] \in D, \phi$ is a conformal map with $\phi : D \to D_d$

2. $\psi = \phi^{-1}$

3. $\rho = e^{\phi(z)}$

4. $\gamma_k^{(h)} = \text{sinc}\left(\frac{\phi(x)-kh}{h}\right)$

Let $\alpha > 0$, and let $L_\alpha(D)$ denote the family of functions F with the properties

- F is analytic in D

- for some $c > 0$ and all $z \in D$,

$$|F(z)| \le c\frac{\rho(z)^\alpha}{(1+|\rho(z)|)^{2\alpha}} \qquad (20)$$

Now, taking $h = \left(\frac{\pi d}{\alpha N}\right)^{1/2}$, we have the interpolation result

$$f(x) = \sum_{k=-N}^{N} c_k \gamma_k^{(h)}(x) + E(N)$$

$$E(N) = C\sqrt{N}e^{-\sqrt{\pi d \alpha N}} \qquad (21)$$

for a positive c_1 depending only on f, d and α. Notice that equation 20 requires f to vanish at the endpoints of the interval.

As before, this series can be enhanced to handle nonhomogeneous endpoint values with a simple addition:

$$F(x) = \sum_{k=-M}^{N} c_k \gamma_k^{(h)}(x) + c_{N+1}S_b(x) + c_{-M-1}S_a(x) + E(M, N) \qquad (22)$$

$$c_k = (F - S_a - S_b)(\psi(kh)), k = -N..N \qquad (23)$$
$$c_{N+1} = F(b) \qquad (24)$$
$$c_{-M-1} = F(a) \qquad (25)$$

8

and S_a and S_b are cubic splines with value 1 at the left and right endpoints, respectively, and zero derivatives at the endpoints.

As written, the expressions for the c_k are no longer simple function evaluations. This extra work can be shifted to the expansion of F by defining the discrete-orthogonal terms

$$\hat{S}_a(x) = S_a(x) - \sum_{k=-M}^{N} d_k \gamma_k(x) \tag{26}$$

$$d_k = S_a(\psi(kh)) \tag{27}$$

$$\hat{S}_b(x) = S_b(x) - \sum_{k=-M}^{N} d_k \gamma_k(x) \tag{28}$$

$$d_k = S_b(\psi(kh)) \tag{29}$$

With these definitions, we have the expansion

$$F(x) = \sum_{k=-N}^{N} c_k \gamma_k^{(h)}(x) + c_b \hat{S}_b(x) + c_a \hat{S}_a(x) \tag{30}$$

with $c_k = F(x_k)$, $c_a = F(a)$, $c_b = F(b)$, and $x_k = \psi(kh)$

2.3.1.2 Extensions for mixed boundary value problems   For the solution of mixed boundary value problems, a finite nonzero approximation of the derivative at endpoints is needed. Since the derivatives of the γ_k are unbounded at the endpoint, a nullifier g is introduced to make the derivatives of the series terms also vanish at the endpoints. Then, as before, adding extra terms with the right properties gives a useful basis.

Let $T_a(x)$ and $T_b(x)$ be cubic splines with derivatives of one at the left and right endpoint, respectively, and other values and derivatives zero at the endpoints; then the following series can be used to approximate f on $[a, b]$ when f is specified via a mixed boundary value problem.

$$f(x) = \sum_{k=-M}^{N} c_k \gamma_k(x) + c_b \hat{S}_b(x) + c_a \hat{S}_a(x) + c_{b'} \hat{T}_b(x) + \tag{31}$$

$$c_{a'} \hat{T}_a(x) + E(N, M) \tag{32}$$

$$\gamma_k = \text{sinc}\left(\frac{\phi(x) - kh}{h}\right) g(x) \tag{33}$$

$$x_k = \psi(kh) \tag{34}$$

$$g(x) = \frac{1}{\phi'(x)} \tag{35}$$

$$c_k = f(x_k)/g(x_k) \tag{36}$$

9

$$c_b = f(b) \tag{37}$$

$$c_a = f(a) \tag{38}$$

$$c_{b'} = f'(b) \tag{39}$$

$$c_{a'} = f'(a) \tag{40}$$

$$\hat{S}_a(x) = S_a(x) - \sum_{k=-M}^{N} d_k \gamma_k(x) \tag{41}$$

$$d_k = \frac{S_a(x_k)}{g(x_k)} \tag{42}$$

$$\hat{S}_b(x) = S_b(x) - \sum_{k=-M}^{N} d_k \gamma_k(x) \tag{43}$$

$$d_k = \frac{S_b(x_k)}{g(x_k)} \tag{44}$$

$$\hat{T}_a(x) = T_a(x) - \sum_{k=-M}^{N} d_k \gamma_k(x) \tag{45}$$

$$d_k = \frac{T_a(x_k)}{g(x_k)} \tag{46}$$

$$\hat{T}_b(x) = T_b(x) - \sum_{k=-M}^{N} d_k \gamma_k(x) \tag{47}$$

$$d_k = \frac{T_b(x_k)}{g(x_k)} \tag{48}$$

All following extensions are based upon this series representation, or subsets of it.

2.3.2 Sinc methods extended for 2D problems

The straightforward way to extend the *sinc* series to higher dimensions is via tensor product. In this section, two derivations of the series expansion are given and the matrix structure which arises for collocation is described.

In section 2.3.2.1, we first show the derivation under the assumption that the unknown can be fully represented by the series (31), and using a tensor product to get the two dimensional extension.

Next, we treat the splines in (31) as a change of unknown, so as to produce a homogeneous equation to be satisfied by the simple sum $\sum_{k=-M}^{N} c_k \gamma_k(x)$, and extend this line of thinking to two dimension – section 2.3.2.2.

Extension of the series to multiple domains is considered in section 2.3.2.3

Splitting of the two dimensional series into logical units for collocation and matrix setup is the subject of section 2.3.2.4.

2.3.2.1 Tensor product derivation

Let $u(x)$ be represented by the full sum used in equation (31), written as single sum. Thus

$$u(x) = \sum_{k=-M-2}^{N+2} c_k \gamma_k(x) = c_k \gamma_k(x) \tag{49}$$

where the last equation is written in summation notation (repeat subscripts are summed over). Then we have

$$
\begin{aligned}
u(x,y) &= [d_{k_1}(y)]\,\gamma_{k_1}(x) \\
&= [d_{k_1 k_2}\gamma_{k_2}(y)]\,\gamma_{k_1}(x) \\
&= \sum_{k_1=-M_1-2}^{N_1+2}\sum_{k_2=-M_2-2}^{N_2+2} d_{k_1 k_2}\gamma_{k_1}(x)\gamma_{k_2}(y)
\end{aligned}
\tag{50}
$$

This representation is valid on any rectangular region; regions with other shapes can easily be mapped onto a rectangle. Also, the "rectangle" can be unbounded on one or more sides; only the choice of conformal map (below) changes. Thus, half- or fullspace problems can be solved easily.

Assume for simplicity $N_1 = N_2$, $M_1 = M_2$. Define m as $m = N + M + 1$. Then the series (50) has

$$(m+4)^2 = m^2 + 8m + 16 \tag{51}$$

terms. Notice that this is the most general form possible, used for problems with mixed conditions on all boundaries. Since not every problem has mixed conditions on all boundaries, the nullifier must be selected in conjunction with the splines for each direction and boundary separately before forming the tensor product.

To this end, it is more natural to think of the splines as a remapping of the unknown – the subject of the next section.

For collocation points, starting from $\{x_k | x_k = \psi(kh)\}_{k=-M-1..N+1} \cup \{x_a, x_b\}$ for the one-dimensional case, we get the collocation points as a tensor product also:

$$\{x_{kj} | x_{kj} = (\psi(kh_1), \psi(jh_2))\}_{k=-M_1-1..N_1+1,\,j=-M_2-1..N_2+1} \cup \tag{52}$$
$$\{x_{aj} | x_{aj} = (x_a, \psi(jh_2))\}_{j=-M_2-1..N_2+1} \cup \tag{53}$$
$$\{x_{bj} | x_{bj} = (x_b, \psi(jh_2))\}_{j=-M_2-1..N_2+1} \cup \tag{54}$$
$$\{x_{ka} | x_{ka} = (\psi(kh_1), y_a)\}_{k=-M_1-1..N_1+1} \cup \tag{55}$$
$$\{x_{kb} | x_{kb} = (\psi(kh_1), y_b)\}_{k=-M_1-1..N_1+1} \tag{56}$$

Notice that we have $(m+4)^2 = m^2 + 8m + 16$ points, as expected.

2.3.2.2 Tensor products revisited

Recall the simple series used for L_α functions in 1D (equation (21)). By using a nullifier, this series has zero value and

11

zero derivative at the boundaries. By providing splines for the nonhomogeneous boundary conditions (equation (22)), the problem $Lu = f, Bu = g$ is effectively remapped to $Lv = \tilde{f}, Bv = 0$ and this problem can be solved with the sinc-only series (21).

The same approach can be taken in 2 (and higher) dimensions. Starting with the simple sinc series and forming the tensor product, we obtain the representation

$$u(x, y) = \sum_{j=-M_1}^{N_1} \sum_{k=-M_2}^{N_2} c_{jk} \cdot (S(k, h_1) \circ \phi_1 g_1)(x)(S(j, h_2) \circ \phi_2 g_2)(y) \quad (57)$$

valid for $u \in L_\alpha$, $u'(a) = u'(b) = 0$. It thus remains to remap the problem $Lu = f, Bu = g$ to $Lv = \tilde{f}, Bv = 0$.[2] Taking a hint from the previous section, on each boundary of the rectangle, we can use a series of the form

$$\sum_{j=-M_1}^{N_1} \left[(S(k, h) \circ \phi_1 g_1)(x_1) + \hat{S}_a(x_1) + \hat{S}_b(x_1) + \hat{T}_a(x_1) + \hat{T}_b(x_1) \right] \hat{S}(x_2) \quad (58)$$

for u's value and tangential derivative, and a series of the form

$$\sum_{j=-M_1}^{N_1} \left[(S(k, h) \circ \phi g)(x_1) + \hat{S}_a(x_1) + \hat{S}_b(x_1) \right] \hat{T}(x_2) \quad (59)$$

for $\frac{\partial u}{\partial n}$. The direction of the boundary is x_1, the normal direction x_2. This gives a total of $m^2 + 8m + 24$ terms per unknown. The causes for this larger number are redundancies at the corners of the domain, in the spline-only terms. First, u only has one value at each corner, reducing the total number of terms by 4. Then, the x and y partials at each corner are unique also, further reducing the number of terms by 8. Thus, we are left with $m^2 + 8m + 12$ terms per unknown. The four terms missing here but present in (50) are the second order mixed derivative terms representing $\frac{\partial^2}{\partial x \partial y}$ at the corners of the domain.

The results in sections 2.3.2.1 and 2.3.2.2 thus differ at the corners of the domain; numerically, the presence of terms representing the mixed second partial is redundant and these terms are not used.

Next, we derive at the collocation points by extending the 1D problem in a way analogous to the series derivation, rather than by tensor product. First, recall that for 1D, three point regions can be distinguished. Always present are interior collocation points, given by $x_k = \psi(kh), k = -M..N$ since these correspond to the *sinc* part of the series. When the splines representing the

---

[2]Note: for single unknown problems, an explicit remapping can usually be found, so that the resulting problem has only the coefficients of (57) as unknowns. However, with multiple unknowns, only the *form* of the remapping is known, and unknown coefficients of this form also go into the matrix system. Thus, this approach is somewhat implicit.

Figure 5: The point layout for 2D collocation, for $N = M = 1$. The circles are the boundary points, while the crosses represent the always present part of the interior points obtained from the 1D tensor product. The points marked with triangles are used only when the derivative spline terms corresponding to them are present. Notice that the points are not really evenly spaced.
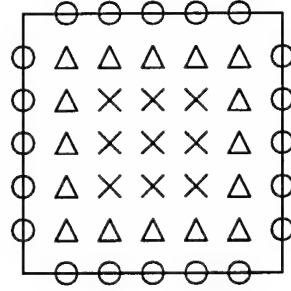
value of the unknown at the endpoints of the interval are present ($\hat{S}_{x_a}$ etc.), the collocation point set is expanded to include the boundary points. Lastly, when the splines representing the derivatives at endpoints ($\hat{T}_{x_a}$ etc.) are included, the collocation points are further extended with extra points in the interior: $x_k = \psi(kh), k = \{-M - 1, N + 1\}$

Selecting the collocation points in 2D analogously we have a point grid as shown in figure 5.

Notice that here we have no points at the corners, unlike equations (52); this is consistent with the series selection in equations (57) through (59), since there we also have 4 terms fewer than equation (50).

2.3.2.3 Multiple Domain problems in 2D

Handling of multiple domain problems is straightforward. At the connecting boundaries, the equations involve unknowns from both domains and this simply reflects in the collocation matrix.

Stated another way, the continuous properties of the linear problem are reflected in the discrete approximation via the linear system. Therefore, one has to only consider the matrix implications of domain coupling. These considerations go along with those for general matrix setup, and are the topic of section 2.3.2.4.

2.3.2.4 Splitting of the series and points

Recollecting the form of the series in section 2.3.1.2 (equation 31), we next expand the pieces of equations (57) through (59) and arrange the terms in a form conducive to setting up and solving the linear system which arises from collocation of a boundary value problem.

Similarly, the collocation points in figure 5 are dealt with in separate parts,

13

to facilitate multiple domain handling and more elaborate unknown representations[3].

For collocation point ordering, first note that different equations are valid on each of the boundaries, and further that not all of the ancillary interior points (triangles, figure 5) are always needed, while the interior points (crosses, figure 5) are always used. This suggests separately handling the boundaries, ancillary interior points, and interior points, giving a total of six point sets per domain. Throughout, these will be denoted by t,b,l,r,a,i.

For the unknown's component splitting, note the following.

- The Spline-Spline product terms are nonzero in most of the point regions.

- The interior series has zero value and derivative, or zero value and unbounded derivative (depending on nullifier) on the boundaries, and thus never needs to be explicitly evaluated at there.

- The Series-Spline terms of equation (58) and (59) are nonzero only in the interior and *their* boundary (the boundary on which the spline's value or derivative is 1)

From these observations, it follows that for multiple domains, only the Spline-Spline product terms and the Series-Spline terms on the touching boundaries are affected by the overlap, and the domains unknowns' are otherwise independent. Thus, the unknowns are split into top-value, top-partial, left-value, ..., right-partial and interior series parts, complemented by the Spline-Spline terms, which we will refer to as corner splines (since they provide values and derivatives at the corners).

This is perhaps best illustrated pictorially; figure 6 shows the structure of a single unknown using formulas, while figure 7 shows the structure as it is implemented on the computer.

The above structuring for points and unknowns leads directly to the matrix block structure. Since this structure can only be drawn for specific cases, we refer here to figure 11 which is part of the example shown later.

2.3.2.5 Numerical Example – Multiple Unknown/Domain problem   This is one of many test problems; it is far from the hardest. It was chosen here because it illustrates all important features of the *sinc* method applied to multiple-domain, multiple-unknown P.D.E. problems, while being conceptually simple.

---

[3]Mixed boundary conditions on one boundary, with Dirichlet or Neumann conditions on another, and coupling between unknowns and domains.
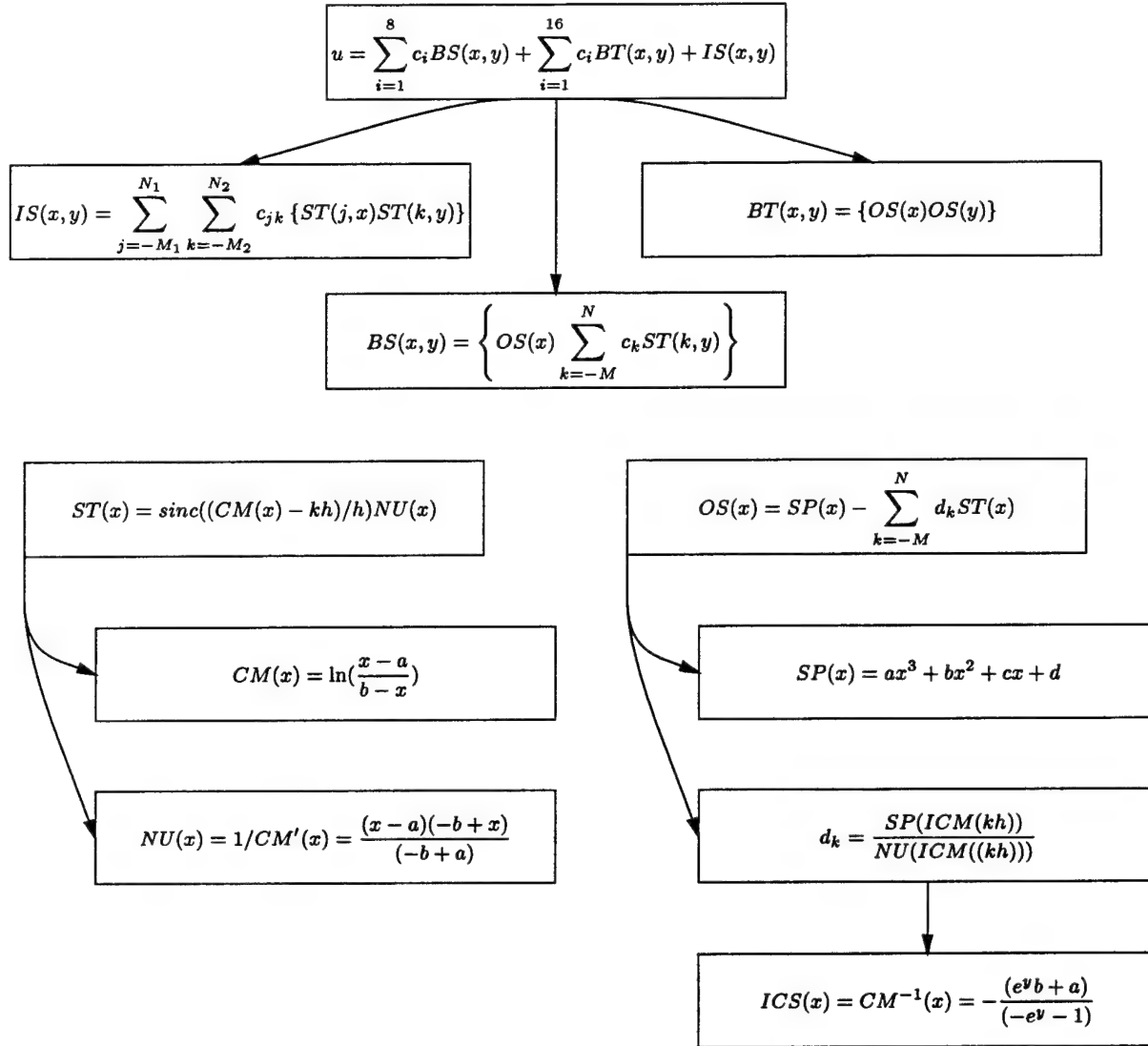
$$u = \sum_{i=1}^{8} c_i BS(x,y) + \sum_{i=1}^{16} c_i BT(x,y) + IS(x,y)$$

$$IS(x,y) = \sum_{j=-M_1}^{N_1} \sum_{k=-M_2}^{N_2} c_{jk} \{ST(j,x)ST(k,y)\}$$

$$BT(x,y) = \{OS(x)OS(y)\}$$

$$BS(x,y) = \left\{ OS(x) \sum_{k=-M}^{N} c_k ST(k,y) \right\}$$

$$ST(x) = sinc((CM(x) - kh)/h)NU(x)$$

$$OS(x) = SP(x) - \sum_{k=-M}^{N} d_k ST(x)$$

$$CM(x) = \ln(\frac{x-a}{b-x})$$

$$SP(x) = ax^3 + bx^2 + cx + d$$

$$NU(x) = 1/CM'(x) = \frac{(x-a)(-b+x)}{(-b+a)}$$

$$d_k = \frac{SP(ICM(kh))}{NU(ICM((kh)))}$$

$$ICS(x) = CM^{-1}(x) = -\frac{(e^y b + a)}{(-e^y - 1)}$$

Figure 6: The unknown's representation hierarchy (mathematical expressions shown).

The Geometry

This problem requires the solution of two sets of elliptic partial differential equations on two rectangles which have one common boundary. See figure 8 for the equations and their location. In the equations, the following definitions are used:

$$\sigma_{xx} = (\lambda + 2G) \frac{\partial}{\partial x} u + \lambda \frac{\partial}{\partial y} w \qquad (60)$$

$$\sigma_{yy} = (\lambda + 2G) \frac{\partial}{\partial y} w + \lambda \frac{\partial}{\partial x} u \qquad (61)$$

$$\sigma_{xy} = G \frac{\partial}{\partial x} w + G \frac{\partial}{\partial y} u \qquad (62)$$

15
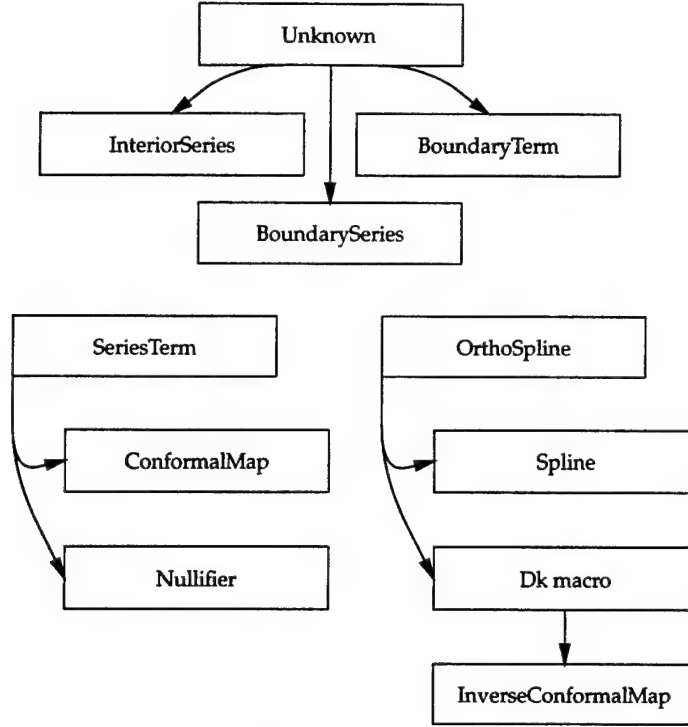
Figure 7: The unknown's representation hierarchy (program parts shown).

and g_1 etc. are determined by substitution of the exact answer, chosen below, into the appropriate equation.

The exact answers

The exact answers here are chosen as

$$u1 = (x - x_a)^{lpu1} (x_b - x) \tag{63}$$

$$w1 = (x - x_a)^{lpw1} + 3.0 \tag{64}$$

$$u2 = (y - y_a)(y_b - y) + (x_b - x)^{rpu2} \tag{65}$$

$$w2 = (y - y_a)(y_b - y)(x - x_a)(x_b - x)^{rpw2} \tag{66}$$

and runs are made for various values of $lpu1$, $lpw1$, $rpu2$, $rpw2$. x_a and y_a denote the left and bottom boundary of the domain, respectively, while x_b and y_b denote the right and top boundaries.

Numerical Parameter Values

For the above equations, the parameter values shown in tables 1 were used.

Parameters of Unknowns' Sum Representation

Having the unknowns' representation as detailed in section 2.3.2.4, it remains to provide parameter values; the chosen parameters are shown in table 2.

Collocation Points Used

In figure 9, the used collocation points' indices are shown graphically. Recall

16
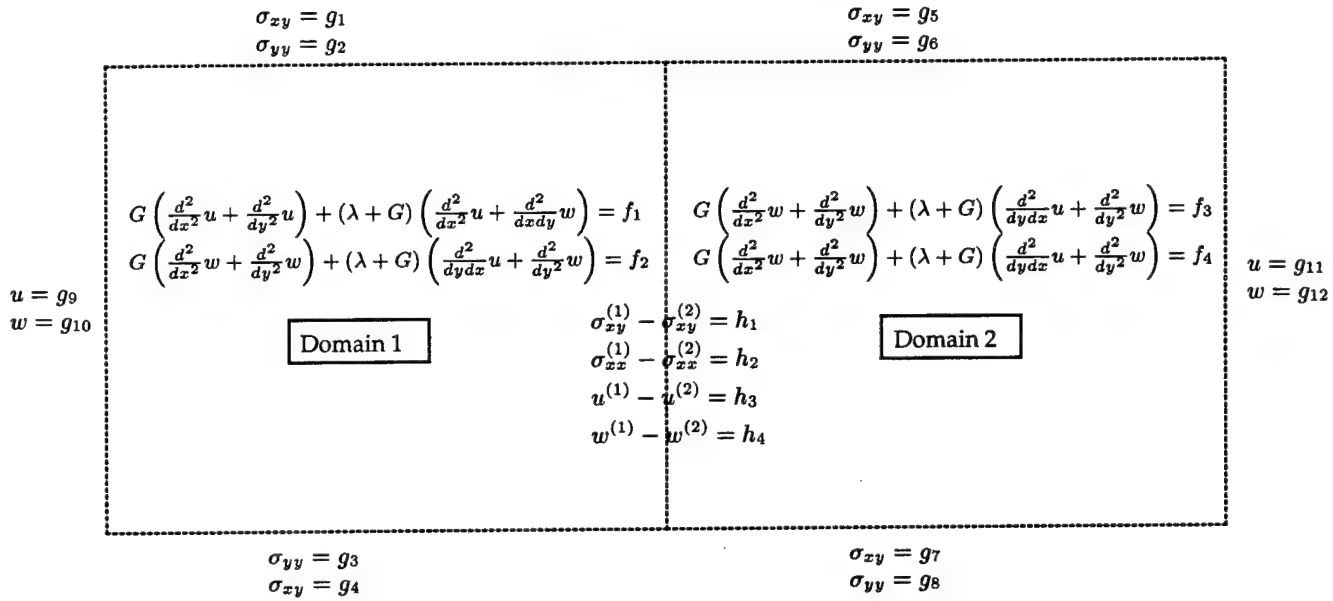
Figure 8: Domains with equations.

Table 1: Equation parameters

domain 1:	domain 2:
$x_a = 1.0$	$x_a = 2.0$
$x_b = 2.0$	$x_b = 3.0$
$y_a = 1.0$	$y_a = 1.0$
$y_b = 2.0$	$y_b = 2.0$
$G = 1.1$	$G = 1.1$
$\lambda = 2.0$	$\lambda = 2.0$

that the actual position of a point is given by

$$x_j = \phi^{-1}(jh_1), \ y_k = \phi^{-1}(kh_2)$$

and interior points are "bunched up" near the boundaries.

The block matrix
The above formulas are used to set up a matrix corresponding to the original linear PDEs; its structure is shown with fixed block sizes (to keep names legible) in figure 10, and in proportion in figure 11

Some numerical comparisons
There are many graphs for even this single problem. Some representative results are shown in figures 13, 12 and 14.These graphs show slices in the y direction, displayed to fit on single pages. Results shown use 29 series terms in both x and y directions, and were computed on a PC with 32 Megabytes

17

Table 2: Parameters for the *sinc* sum, both domains.

$$d = \pi/2.0$$
$$\alpha = 1.0$$
$$M_1 = 10$$
$$M_2 = 10$$
$$N_1 = 10$$
$$N_2 = 10$$
$$M_1 = M_1 + N_1 + 1$$
$$M_2 = M_2 + N_2 + 1$$
$$h_1 = \sqrt{\frac{\pi d}{\alpha N_1}}$$
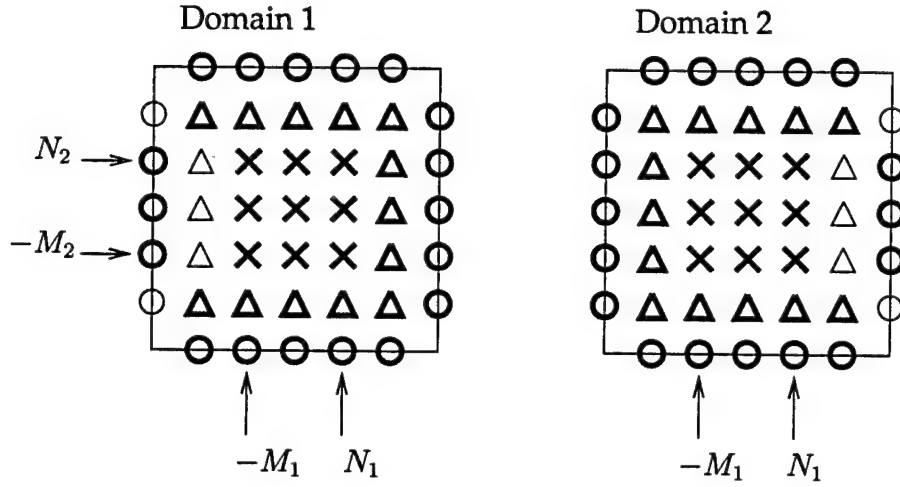$$h_2 = \sqrt{\frac{\pi d}{\alpha N_2}}$$

Figure 9: All possible collocation points are shown, but only boldface ones are used in this example.

of memory.

Because the accuracy at most points exceeds 2 digits, most graphs show no visible errors; the partial derivative in x shown in figure 13 has roughly a 10% relative error on the y-slice $x = 1.001$ near the left boundary of the domain. Not shown is the relative error on the y-slice at $x = 1.003$, only around 1%. Put another way, we can expect less than 1% relative error when within 3/1000 of the singularity or crack, using sufficiently many terms in the series. This is close enough, for example, to curve fit a simplified local model of singular behavior near the crack tip, if so desired.

In conclusion, we thus get very good uniform accuracy, for functions and derivatives, with both bounded and unbounded derivatives, making the method well suited for crack and related problems.

Figure 10: Coupled problem. Entries have the form ⟨unknown⟩–⟨equation⟩–⟨domain⟩–pts–⟨point region⟩–prt–⟨unknown part⟩.

19

Figure 11: Coupled problem, to scale, $M = N = 10$.
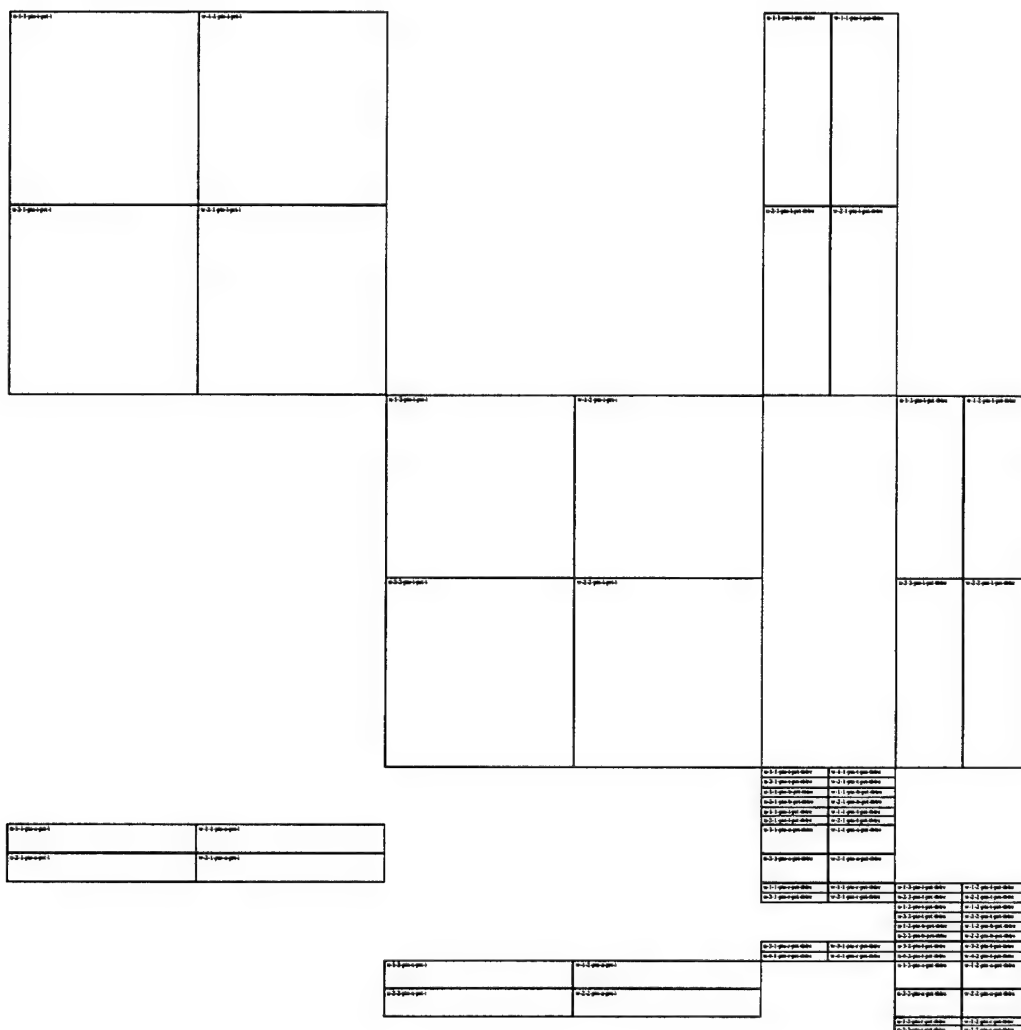
Figure 12: Function value comparison; stars are computed values, solid lines are the exact answer.

Sum/Exact. domain: 1 unknown: u   M1 = 14

y slices at indicated x values. y ranges from 1.001 to 1.997

Figure 13: Comparison of function's partial derivative in x; stars are computed values, solid lines are the exact answer.

Sum/Exact. domain: 1 unknown: u, x partial, M1 = 14
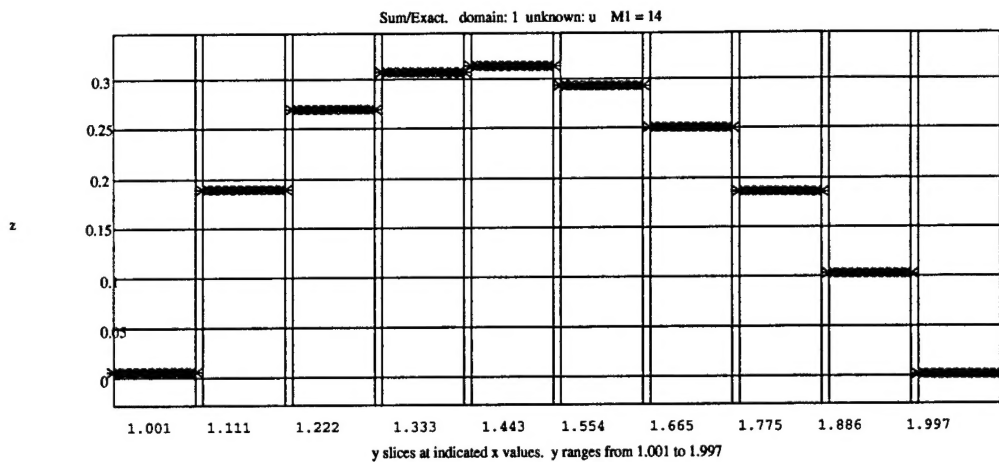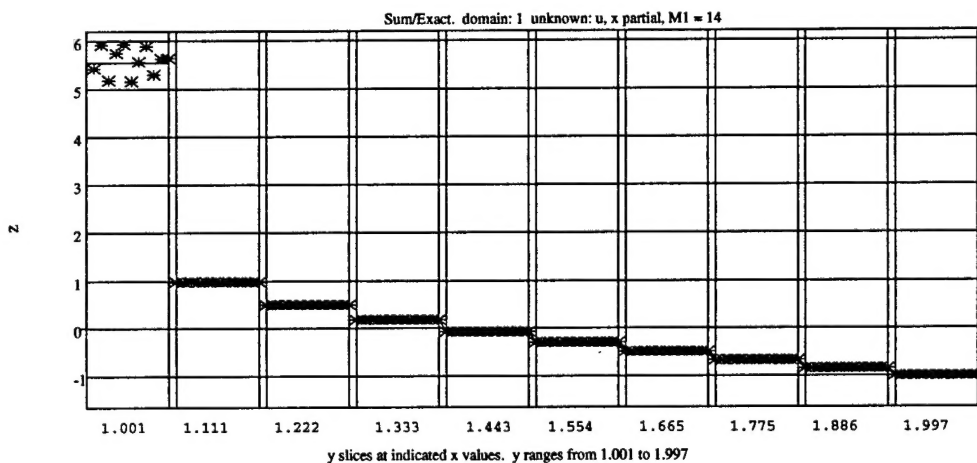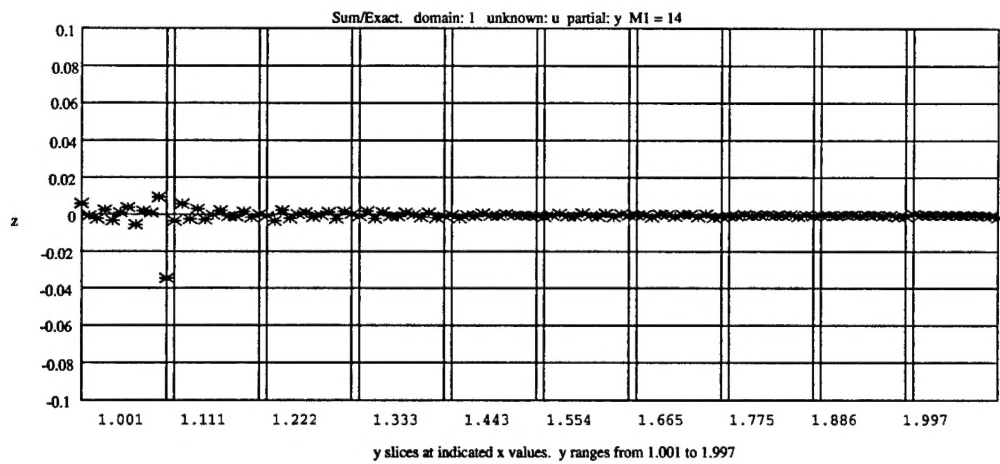
y slices at indicated x values. y ranges from 1.001 to 1.997

21

Figure 14: Comparison of function's partial derivative in y; stars are computed values, solid lines are the exact answer.

Sum/Exact. domain: 1 unknown: u partial: y M1 = 14

y slices at indicated x values. y ranges from 1.001 to 1.997

REPORT DOCUMENTATION PAGE

1a. REPORT SECURITY CLASSIFICATION **Unclassified**	**1b. RESTRICTIVE MARKINGS**
2a. SECURITY CLASSIFICATION AUTHORITY	**3. DISTRIBUTION/AVAILABILITY OF REPORT** Approved for public distribution; distribution unlimited.
2b. DECLASSIFICATION/DOWNGRADING SCHEDULE	
4. PERFORMING ORGANIZATION REPORT NUMBER(S)	**5. MONITORING ORGANIZATION REPORT NUMBER(S)**

6a. NAME OF PERFORMING ORGANIZATION **Department of Mathematics** **University of Utah**	**6b. OFFICE SYMBOL** *(If applicable)*	**7a. NAME OF MONITORING ORGANIZATION** AFOSR/NA
6c. ADDRESS (City. State and ZIP Code) **Salt Lake City, Utah 84112**		**7b. ADDRESS (City. State and ZIP Code)** 110 Duncan Ave, Ste 115 Bolling AFB, DC 20332-8050
8a. NAME OF FUNDING/SPONSORING ORGANIZATION **AFOSR**	**8b. OFFICE SYMBOL** *(If applicable)*	**9. PROCUREMENT INSTRUMENT IDENTIFICATION NUMBER** F496209310074 (P00002)

8c. ADDRESS (City. State and ZIP Code) **Bolling A.F.B, Washington D.C. 20332-0001**	**10. SOURCE OF FUNDING NOS.**			
	PROGRAM ELEMENT NO.	**PROJECT NO.**	**TASK NO.**	**WORK UNIT NO.**
11. TITLE LOAD TRANSFER CHARACTERISTICS AND RESIDUAL STRESSES IN COMPOSITE MATERIAL SYSTEMS				

12. PERSONAL AUTHOR(S)
Final Technical Report E. S. Folias

13a. TYPE OF REPORT	**13b. TIME COVERED** FROM 1 Dec 92 TO 30 Sep 96	**14. DATE OF REPORT (Yr., Mo., Day)** 1996, Dec. 31	**15. PAGE COUNT** 25

16. SUPPLEMENTARY NOTATION

17.	**COSATI CODES**		**18. SUBJECT TERMS (Continue on reverse if necessary and identify by block number)**
FIELD	**GROUP**	**SUB. GR.**	

19. ABSTRACT (Continue on reverse if necessary and identify by block number)

I . In this study, the load transfer characteristics of a broken fiber are investigated. The problem consists of a cylindrical fiber that is embedded into a matrix material. The fiber axis is assumed to coincide with the z-axis and a crack is assumed to be present on the plane $z = 0$ and for $r < a$. Far away from the crack, the fiber is subjected to uniform external load of σ_o.

Moreover, adjacent to the crack and along the interface, the matrix and fiber surfaces are assumed to slide along the interface length $-c < z < c$, where there is a non-uniform friction $\tau_{rz}^{(f)} = \mu \sigma_{rr}^{(m)}$. On the other hand, perfect bonding is assumed to prevail all along the remaining interface, i.e. for $|z| > c$.

20. DISTRIBUTION/AVAILABILITY OF ABSTRACT UNCLASSIFIED/UNLIMITED ☒ SAME AS RPT. ☐ DTIC USERS ☐	**21. ABSTRACT SECURITY CLASSIFICATION** **Unclassified**	
22a. NAME OF RESPONSIBLE INDIVIDUAL E. S. Folias	**22b. TELEPHONE NUMBER** *(Include Area Code)* 801-581-8124	**22c. OFFICE SYMBOL**

DD FORM 1473, 83 APR   EDITION OF 1 JAN 73 IS OBSOLETE.   SECURITY CLASSIFICATION OF THIS PAGE

II. Residual stresses due to curing and thermal stresses due to differences between the thermal expansion coefficients of the matrix and fiber may have a major effect on the microstresses within a composite material system and must be added to the stresses induced by the external mechanical loads. Such microstresses are often sufficient to produce microcracking even in the absence of external mechanical loads, example during the cooling process.

In this report a few selected results are presented for a material system consisting of SIC-6 cylindrical fibers which are periodically embedded into a plate matrix consisting of beta21 material. The results are based on a linear elastic micromechanics model which provides the stress profiles due to (i) a uniform load perpendicular to the direction of the fibers and (ii) due to a thermal expansion mismatch.